

Global stability analysis of an idealized compressor blade row. I. Single-blade passage analysis

Anton Glazkov

Mechanical Engineering, Physical Science and Engineering Division, KAUST, Thuwal 23955, Saudi Arabia

Miguel Fosas de Pando

*Departamento Ingeniería Mecánica y Diseño Industrial, Escuela Superior de Ingeniería,
Universidad de Cádiz, Puerto Real 11519, Spain*

Peter J. Schmid *

Mechanical Engineering, Physical Science and Engineering Division, KAUST, Thuwal 23955, Saudi Arabia

Li He

Department of Engineering Science, University of Oxford, Oxford OX1 3PJ, United Kingdom



(Received 13 December 2022; accepted 25 May 2023; published 11 October 2023)

A direct-adjoint mean flow global stability investigation of self-excited instabilities in an idealized, two-dimensional compressor blade row at off-design conditions is carried out, with a focus on acoustic feedback mechanisms underlying the observed instabilities. This paper is the first part of this work, where nonlinear flows, impulse responses and the global modes are computed for a single-passage system, with good agreement between the linear and nonlinear structures. Structural sensitivities and feedback loops are identified with the aid of wavemakers and show that dominant structures arise due to feedback mechanisms linking the pressure and suction sides of the aerofoil via acoustic waves emanating from the trailing edge. A separate, second part extends this analysis to multiple-blade passages per period window by exploiting the theory of block-circulant matrices and Bloch-wave theory.

DOI: [10.1103/PhysRevFluids.8.103903](https://doi.org/10.1103/PhysRevFluids.8.103903)

I. INTRODUCTION

Increasingly stringent emissions regulations are presenting novel challenges to the turbomachinery community. With the need to produce more efficient, lighter, and quieter aeroengines, this requires additional understanding of flow instabilities and unsteady flow phenomena present in the various components of the turbomachine [1]. Despite these prominent goals, early-stage design in industry still relies mostly on steady-state Reynolds-Averaged Navier Stokes (RANS) models over a single passage that capture the aerodynamics—but not the instabilities. Access to computationally efficient models, as well as an in-depth understanding of the instabilities and their

*Corresponding author: peter.schmid@kaust.edu.sa

Published by the American Physical Society under the terms of the [Creative Commons Attribution 4.0 International](https://creativecommons.org/licenses/by/4.0/) license. Further distribution of this work must maintain attribution to the author(s) and the published article's title, journal citation, and DOI. Open access publication funded by King Abdullah University of Science and Technology.

feedback mechanisms, is mandatory for optimizing these systems and for eventually achieving the specifications outlined in the regulations.

Modal and nonmodal analyses provide a powerful framework for the analysis of these systems [2,3] and have been applied to a wide variety of flow problems with some considerable success. Of these, perhaps the most used in industrial settings are the data-driven modal-decomposition approaches of the proper orthogonal decomposition (POD) [4], its spectral, frequency-based counterpart (sPOD), and the dynamic mode decomposition (DMD) [5]. These have been applied extensively in turbomachinery contexts, with success of these methods largely attributable to the fact that they may be applied to both numerical and experimental data directly, using snapshots of the nonlinear flow solution or observations of the flow. Many comprehensive reviews demonstrating the theory, strengths and weaknesses [3], and the application [6] of these methods exist. Although these methods offer a convenient, and frequently the only, option for a modal decomposition of the flow, perhaps their greatest shortcoming is that they fail to provide any direct indication of the structural sensitivities of the various modal structures that are obtained. For numerical studies, however, the availability of a linearized component (i.e., the direct linear operator) can be used to address this issue, which ultimately enables global stability analyses to be carried out [7].

The global modes approach is most familiar in the context of steady base flows undergoing transition to instability, with early forays into stability theory starting with the study of simple flows at low Reynolds numbers [7]. By contrast, the vast majority of flows in turbomachinery are highly unsteady, with conditions taking the flow well beyond criticality. Under these circumstances, the argument for the application of classical stability theory around steady base flows becomes increasingly tenuous. Recent developments have instead considered time-averaged mean flows as the linearization state. Unlike steady base flows, these always exist, but are no longer the equilibrium states of the Navier-Stokes equations. It has been shown in [8] that this analysis remains valid, however, since important nonlinearities of the flow field are accounted for in the establishment of the mean flow. For this reason, many studies that have attempted mean-flow global stability analyses of fuel injectors [9,10], jets [11], and aerofoils [12,13], have shown very good agreement between both the spatial structures and their corresponding temporal frequencies when compared to the spectrum of the nonlinear flow field. Furthermore, the adjoint of the direct operator, which is equivalently to the Hermitian conjugate of the direct linear system, can provide additional structural sensitivity information for the given global modes [14–17] and has seen great utility in many turbomachinery optimization applications [18,19] and sensitivity analyses [13]. Two versions of the adjoint approach exist: the continuous [20] and the discrete [21], with the latter preferred here for consistency with the discretized direct operator. Moreover, it is also worth highlighting that for many flow problems the Navier-Stokes operator in the large Reynolds number regime is highly nonnormal, the result of which is that it has the potential to support large-scale transient dynamics that differ considerably from the asymptotic behavior obtained from the global modes [22]. The flow considered in this study is no exception in this respect. For this reason, performing an impulse response analysis prior to calculating the spectrum and the corresponding eigenvectors appears to be a prudent step to evaluate the effects that nonnormality has on the flow.

The demonstration problem selected in our analysis is inspired by previous flow receptivity studies conducted on isolated aerofoils, which we use here and apply to simplified cascade geometries to demonstrate this methodology. Briefly, earlier work [23] identified the presence of discrete tones on isolated aerofoils and suggested empirical laws for the evolution of the main peak for the tonal noise structure. Theoretical and experimental work by Tam, Fink, Nash, and others [24–27] later proposed that the presence of these discrete tones can be attributed to localized acoustic feedback mechanisms linking the acoustic source at the trailing edge to the upstream boundary layers of the aerofoil, with subsequent numerical work considering this problem on a NACA 0012 profile [28,29] and controlled-diffusion geometries [30,31]. In his earlier work, Fosas de Pando [12] analyzed this tonal noise problem with the NACA 0012 aerofoil and performed a global stability analysis that correlated these tonal noise peaks to global mode structures. Later calculations [13] extended this analysis using adjoint techniques and wavemaker analysis, and showed that both the pressure and suction

sides of the aerofoil participate, though to varying degree, in setting the feedback mechanisms. This latter analysis serves as the inspiration for the work carried out here.

The geometry and flow conditions are chosen so that the flow exhibits many of the qualitative flow features that are present in more realistic settings. These include oscillating laminar separation bubbles that form under adverse pressure gradients on the aerofoil suction side, unsteady boundary layers on the pressure surface, trailing-edge shedding processes, inhomogeneous mean-flow density gradients, and acoustic scattering from both the leading and trailing edges. Nevertheless, in this study, we are limited to considering linear cascades consisting of two-dimensional midspan sections at modest flow regimes. In reality, turbomachinery flows show significantly more complex flow behavior, due to three-dimensional processes and higher Reynolds and Mach numbers. While this constrains a direct translation between the findings of this paper and the industrial design process, the goal here is not only to demonstrate the stability analysis framework, but also to inform the reader of potentially critical phenomena that may soon be within reach of this methodology in future large-scale LES and DNS simulations that can capture this additional complexity.

This paper is split into two parts. In the first part of this study, Sec. II introduces the representative compressor cascade flow case on which the global stability analysis is to be performed, with further details of the compressible, viscous Navier-Stokes solver, its linear counterpart, and the methodology for obtaining the global modes concluding this section. The single-passage case is then considered in Sec. III, so that the *local* feedback mechanisms over one blade can be identified. Here the nonlinear flow field is analyzed using a global Fourier transform in Sec. III A, which identifies the main features of the acoustic spectrum for this problem, and the mean flow is obtained and described in Sec. III B. A linearization around this state is performed, and an impulse response analysis carried out in Sec. III C, to identify transient growth effects that occur due to the operator's nonnormality. Following this, the global modes are calculated in Sec. III D, the spectrum analyzed and decomposed into groups of modes that capture distinct families of behavior for the dominant modes in Sec. III E 1, for the high-frequency separation bubble dynamics in Sec. III E 2 and for confined mode structures in Sec. III E 3. The consideration of the single passage concludes with a phase and group velocity analysis in Sec. III F, which seeks to determine relationships between the different modes within the global spectrum.

In part II of this publication [32], the above analysis is extended to a ten-periodic blade row using the algebraic method introduced by [33]. Details of the geometry and implementation are provided, respectively. This is followed once again by an impulse response analysis and a global stability analysis, where particular emphasis is directed towards synchronization effects across multiple-blade passages.

II. NUMERICAL METHODOLOGY

A. Geometry

The single-passage geometry consists of an idealized controlled-diffusion compressor blade developed by [34,35] and later used in a low-speed aero-elasticity experiment [36]. All simulations presented here are performed at a chord-based Reynolds number of $Re = 100\,000$ and an exit Mach number of $M = 0.3$. The inlet flow angle is set to $\theta_{in} = 37.5^\circ$ to match the inlet angle of the blades, and the nondimensional pitch length for the periodic boundary of the linear cascade is set to $h_p = 0.6$. These flow conditions are adapted from an experiment and previous numerical studies [37,38] by decreasing the Reynolds number from $Re = 195\,000$, and increasing from $M = 0.05$, so that a coarser mesh, and consequently faster time stepping, could be used to increase calculation speed. This choice of parameters also enables us to model the larger, more demanding cases in part II of the paper. Furthermore, as the purpose of this study is to also develop and demonstrate the numerical framework, the adjustments in the Reynolds and Mach numbers are chosen for numerical convenience to expedite the numerical calculations rather than to make definitive statements regarding the flow properties of the aerofoil at the experimental conditions. Nonetheless, the new

TABLE I. Single-passage mesh parameters.

Parameter	Grid A	Grid B	Grid C
n_{upstream}	540	576	1080
$n_{\text{downstream}}$	540	680	1080
n_{airfoil}	680	840	1360
n_{vertical}	256	256	512
L_{upstream}	3.075	3.233	3.075
$L_{\text{downstream}}$	4.024	4.250	4.024
y^+	1.4	0.8	0.7

conditions are chosen so that the main mean flow features, in particular the laminar separation bubble on the suction side and its location, match qualitatively the experiment and the exhibited dynamics are *qualitatively similar*. This will be discussed further in Sec. II B.

The flow field is discretized on a structured H grid, with the mesh parameters given in Table I, and the computational domain shown in Fig. 1. Of these, Grid A is used for all numerical calculations, while Grids B and C were used for the grid independence study, the exhaustive details of which are presented in [39]. To remain consistent with the analysis performed later in part II, the axial lengths of the upstream and downstream sections of this grid are fixed at $L_{\text{upstream}} = 3.075$, $L_{\text{downstream}} = 4.024$. Vertical refinement of the mesh in the downstream section is also gradually smoothed over $L_{\text{smoothing}} = 1.5$ so that unsteady wake structures are represented with sufficient resolution everywhere in the downstream region. Periodic conditions are applied along the top and bottom edges of the upstream and downstream meshes, with steady inflow and outflow boundary conditions specified at the left and right sides of the mesh, respectively, in order to match the required flow angle and outlet Mach number. The minimum grid spacing is $\Delta s_0 = 4.78 \times 10^{-4}$, $\Delta s_1 = 1.89 \times 10^{-4}$ at the airfoil surface, with the maximum spacing found in the upstream region

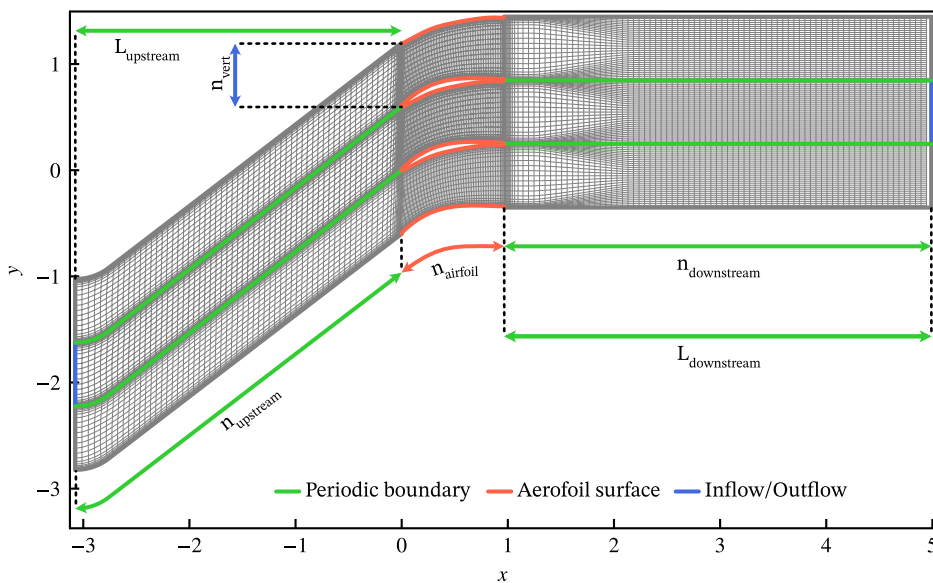


FIG. 1. The single-passage structured grid showing every tenth grid line in each dimension so that the grid metric can be visualized. Boundary conditions are indicated using colored lines.

with $\Delta s_0 = 8.30 \times 10^{-3}$, $\Delta s_1 = 6.39 \times 10^{-3}$, where s_i is the arc-length along direction $i \in 0, 1$.¹ The maximum stretching ratio, $|\Delta s_i - \Delta s_{i-1}|/|\Delta s_{i-1}|$, between consecutive nodes is set to 5%.

At these flow conditions the key unsteady feature is a reattaching laminar separation bubble which forms on the suction side and is centered at $0.55 \times C_{ax}$, where C_{ax} is the axial chord, before reattaching.

Numerical and experimental nonlinear unsteady simulations of this blade have also shown strong vortex shedding from both this detached shear layer and the blunt trailing edge. At higher Reynolds numbers, both the laminar and turbulent solutions of this cascade [37] also show two-dimensional structures within the pressure-side boundary layer which is subject to a positive pressure gradient. These two-dimensional features subsequently turn into Görtler vortices, or streamwise streaks, on the final quarter of the pressure surface, before finally interacting with the trailing edge. Note that these features are absent in the laminar solution in [37], although present in the scale-resolving turbulent flow simulation in [38]. These flow conditions provide rich dynamics under which multiple complex flow features interact and are coupled by the resulting acoustic field arising from the unsteadiness.

B. Numerical simulations

A two-dimensional compressible, high-order Navier-Stokes code based on the pseudo-wave method [40,41] is used for the numerical work in this paper. Advection terms are computed using fifth-order compact upwinding schemes [42], with the dissipation terms differentiated using a compact third-order scheme [43]. A low-storage fourth-order Runge-Kutta method [44] is then used to march the solution forwards in time via the method of lines. Parallelization is achieved using the message passing interface (MPI) [45], so that these codes may be deployed on modern high-performance parallel computing hardware with maximum scaling efficiency.

Direct and adjoint dynamics are obtained from an efficient linearization [46] of the nonlinear code. Matrix-vector multiplications and time-stepping functionalities of this code interface with high-performance linear algebra libraries and solvers integrated into PETSc [47–49] and SLEPc [50] through wrappers providing interfaces to the linearized right-hand side functions.

C. Choice of base flow

Integral to any global stability analysis is the choice of base flow taken as the linearization point around which the linear dynamics are considered. Snapshots of the flow shown in laminar and scale-resolving simulations in [37,38], respectively, and later in Sec. III A, show that the flow field is dominated by instabilities, with no natural steady flow around which a linearization may be taken. Based on the evidence of prior attempts to obtain steady flow states for isolated aerofoil flows (see, e.g., [41]) by reducing the Reynolds number and using stabilization techniques such as selective frequency damping [51], such approaches are likely to lead to large separation regions that do not adequately reflect the realistic flow dynamics in the vicinity of the blade surface. Classical stability analyses performed on steady base flows, derived through these methods, are similarly incapable of accurately modeling the unsteady spatial structures and characteristic frequencies due to the removal of intrinsic nonlinearities that govern the unsteady characteristics of the flow (see the discussion in, e.g., [29]). For this reason, and following from our discussion in the introduction, we select the time-averaged mean flow as the flow state about which to linearize our equations.

This mean flow is computed from the nonlinear flow field once it has reached a quasi-periodic limit cycle on a single periodic passage, for $t \geq 20$. This flow is then averaged over an additional time interval of size $t_T = 30$, so that the flow in the vicinity of the blade surface is converged. Despite this long averaging time, rare vortex-merging phenomena occurring in the downstream region result

¹In other words, $i = 0$ is the horizontal direction, and $i = 1$ the vertical, for a rectilinear Cartesian mesh.

in a far-field mean flow that is not fully converged until much later. This is not considered to be a significant problem, however, since we focus our analysis primarily on the hydrodynamics and acoustics in the vicinity of the aerofoil and in the near wake, with the dominant dynamics expected to occur in these regions.

In studies with higher Reynolds numbers, where the boundary layers are almost fully turbulent, it may be possible to avoid this time-averaging procedure by replacing the mean flow with a RANS-derived base flow, which has been done in many prior studies (see, e.g., [52]). If such an approach is desired, however, a careful comparison between the linear structures and the nonlinear flow must be carried out to ensure that the main structures are accurately represented in such a linear model.

D. Linearization process and linear/adjoint dynamics

1. Linear operators and governing equations

The nonlinear Navier-Stokes equations, partially discretized in space, are written as

$$\frac{d\mathbf{q}}{dt} = \mathbf{F}(\mathbf{q}, t), \quad (1)$$

with \mathbf{F} representing the nonlinear Navier-Stokes operator.

In the discretized framework, the derivatives within \mathbf{F} introduce spatial coupling between individual grid points, which make the naive approach of obtaining the linearization of \mathbf{F} , by sequential perturbations around the mean flow of each degree of freedom, prohibitively expensive. Instead, by treating the derivatives as inputs [41,46], it is possible to break the linearization down into a sequence of block operations. This step significantly speeds up the linearization process, and enables computationally inexpensive access to both the direct, \mathbf{A} , and the adjoint, \mathbf{A}^* , operators. The linear equations are thus given as

$$\frac{d\mathbf{v}}{dt} = \mathbf{A}\mathbf{v} + \mathbf{f}, \quad (2)$$

$$\frac{d\mathbf{w}}{dt} = \mathbf{A}^*\mathbf{w}, \quad (3)$$

with a forcing term \mathbf{f} , which can be used to model the action of a time-dependent physical source on the linear system, such as, for example, harmonic acoustic forcing or an entropy wave. From this point on, Eq. (2) is referred to as the direct equation and Eq. (3) as the adjoint equation. The analysis of the stability properties of the operators \mathbf{A} and \mathbf{A}^* forms the core component of this paper.

2. Choice of inner product

The small-perturbation energy norm for compressible flows [53] is used throughout this study to quantify the magnitude of the linear disturbance. Written in the variables (p, s, \mathbf{u}) , the energy \mathcal{E} of a fluid enclosed by a fixed volume \mathcal{V} is

$$\mathcal{E} = \frac{1}{2} \int_{\mathcal{V}} \left(\frac{1}{\gamma^2 M^2} \frac{p^2}{\bar{\rho}} + \frac{\gamma - 1}{\gamma^2 M^2} \bar{\rho} s^2 + \bar{\rho} \|\mathbf{u}\|^2 \right) d\mathcal{V}, \quad (4)$$

with \bar{p} and $\bar{\rho}$ denoting, respectively, the mean flow² pressure and density.

On a discretized domain, the inner product is

$$\langle \mathbf{w}, \mathbf{v} \rangle_{\mathbf{M}} = \mathbf{w}^H \mathbf{M} \mathbf{v}, \quad (5)$$

²The mean flow can be substituted for any field around which the linearization is taken, such as a steady base flow or a flow snapshot.

where the positive definite matrix $\mathbf{M} = \text{diag}(\mathbf{m}_0, \mathbf{m}_1, \dots, \mathbf{m}_{n-1})$ is block diagonal with

$$\mathbf{m}_i = q \begin{pmatrix} \frac{1}{\gamma^2 M^2} \frac{1}{\bar{\rho}} & 0 & 0 & 0 \\ 0 & \frac{\gamma-1}{\gamma^2 M^2} \bar{\rho} & 0 & 0 \\ 0 & 0 & \bar{\rho} & 0 \\ 0 & 0 & 0 & \bar{\rho} \end{pmatrix}_i |\mathbf{x}(\xi)_i| \Delta\xi \Delta\eta, \quad (6)$$

for $i \in \{0, 1, \dots, n-1\}$, with n denoting the number of grid points in the field, and the determinant $|\mathbf{x}(\xi)|$ describing the scaling between the Cartesian physical and curvilinear computational spaces. With this choice of norm, the fundamental relation

$$\langle \mathbf{A}^* \mathbf{w}, \mathbf{v} \rangle_{\mathbf{M}} = \langle \mathbf{w}, \mathbf{A} \mathbf{v} \rangle_{\mathbf{M}} \quad (7)$$

must be satisfied to machine precision, typically $O(10^{-16})$ on modern computers. From this we can also write the adjoint operator as $\mathbf{A}^* = \mathbf{M}^{-1} \mathbf{A}^H \mathbf{M}$, so that we can perform all calculations with \mathbf{A}^H before scaling this accordingly to obtain the desired properties of \mathbf{A}^* .³

For visualization purposes, the adjoint and wavemaker fields are divided by $\Delta\xi \Delta\eta$ so that the physical amplitudes displayed are independent of the number of grid points, since the discretized form of the inner-product integral in Eqs. (5) and (6) is weighted to account for the integration over the unit square or cube.

E. Integration in time

A general initial-value problem (IVP)

$$\frac{d\mathbf{q}}{dt} = \mathbf{F}(\mathbf{q}, t), \quad (8)$$

$$\mathbf{q}(0) = \mathbf{q}_0 \quad (9)$$

for some initial field \mathbf{q}_0 , is integrated in one of two ways. If \mathbf{F} is nonlinear, a low-storage Runge-Kutta scheme [44] is used to march the solution forward in time at a CFL number of 0.8. Alternatively, if \mathbf{F} is linear, the time integration approximates the exact exponential solution to the linear IVP by using an exponential Krylov timestepping scheme [54]. This scheme is used with a Krylov subspace dimension between 16 and 32 vectors, and with a CFL number of 16.

III. SINGLE-PASSAGE DYNAMICS

A. Nonlinear flow field

We begin by performing a brief analysis of the nonlinear flow field, computed directly using the nonlinear Navier-Stokes solver from Sec. II B. We follow the methodology of Sec. II C and calculate an initial starting flow until $T = 20$, so that the transients arising from the initial conditions are removed. We then continue to integrate in time for 40 additional units with snapshots saved every $\Delta t = 0.02$, resulting in 2000 samples. Positive frequencies⁴ up to $f_{\max} = 24.96$, equivalent to $\text{Im}\{\lambda\}_{\max} \approx 156.8$, with a spectral resolution/bin size of $\Delta f = 0.024$ are resolved with this sampling rate when this field is processed with a fast Fourier transform (FFT). Our choice for the range of frequencies was made by estimating the frequency of the vortex shedding at the separation bubble and at the trailing edge. A snapshot of the nonlinear pressure and dilatation fields is shown in Fig. 2.

³It should be noted that this back-scaling is mandatory on nonuniform grids, since the inner product accounts for the grid metric.

⁴All quantities here are given in nondimensional form in accordance with the nondimensionalization described in [41].

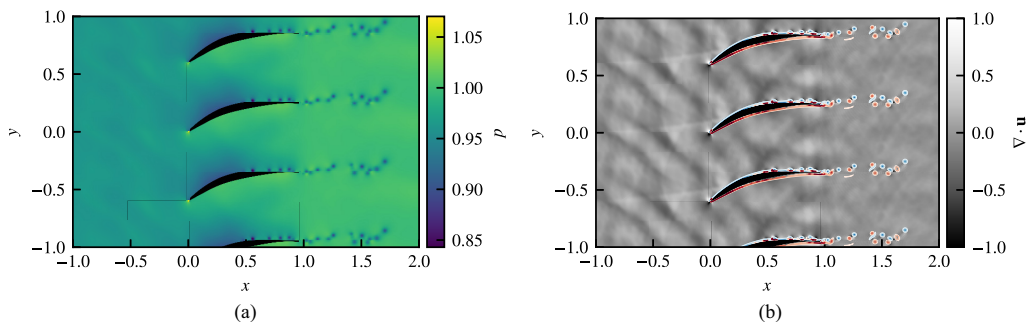


FIG. 2. A snapshot of the (a) nonlinear pressure and (b) dilatation field, with vorticity contours, at $t = 60$. Note the vortex shedding on the suction surface, and the acoustic waves propagating upstream.

These plots demonstrate that the flow unsteadiness at the separation bubble and, subsequently, at the trailing edge results in strong acoustic radiation that is directed primarily upstream through the blade passage and into the inlet portion of the domain. As a consequence, there exists a potential pathway through which the acoustic field can couple and interact with (highly sensitive) regions upstream where the flow first becomes convectively unstable. This feedback mechanism will be analyzed in depth later on when we consider the adjoint and wavemaker fields.

At this point we should acknowledge that, in three-dimensional simulations of this flow, the two-dimensional coherent structures, identified in Fig. 2, will likely break down before the trailing edge. The resulting acoustic field would thus have a broadband spectrum, possibly augmented by the presence of a number of peaks corresponding to the tonal acoustic modes. Despite this concession, prior simulations, particularly in [37,38], indicate that the qualitative structure of the mean flow prior to transition is captured remarkably well by the two-dimensional flow fields shown here, with the laminar boundary layers and the reattaching separation bubble exhibiting qualitatively similar dynamics. As a result, the conclusions made in this paper regarding the receptivity and sensitivities of the laminar boundary layers are likely to be transferable to a three-dimensional setting, at least to some degree. In situations where inlet turbulence or periodic wakes impinge on the blade surface, the two-dimensional behavior may be masked further by more complex transition phenomena and interaction effects, such as bypass transition. However, the two-dimensional analysis that follows would constitute a comparison point against which these three-dimensional effects can be evaluated.

The high-resolution data set described above is used to determine the features of the acoustic spectrum, with the pressure measurements taken at $\mathbf{x} = (-0.228, 0.138)$, which is sited upstream of the blade's leading edge and at the midpoint between the periodic boundaries, and is also situated within the main "lobe" of the upstream-propagating acoustic field (see Fig. 4, where

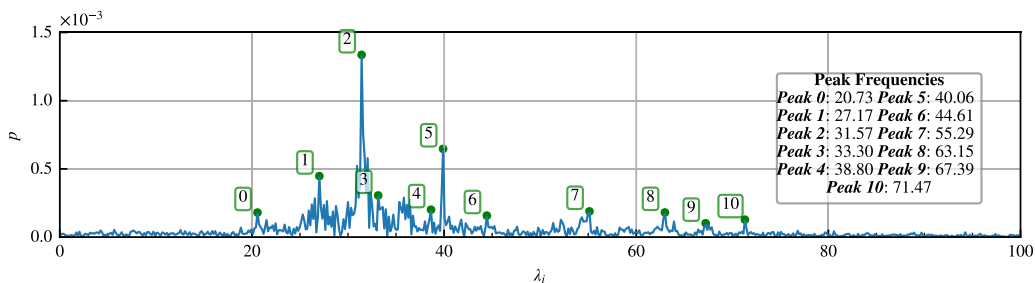


FIG. 3. The fast Fourier transform (FFT) of the acoustic field upstream of the blade's leading edge at $\mathbf{x} = (-0.228, 0.138)$.

this point is shown with a red cross). This spectrum is shown in Fig. 3. The observed spectrum consists of a series of eleven discernible peaks that dominate the pressure field across a range of frequencies from $\text{Im}\{\lambda\} = 20.73$ to 71.47 , suggesting a certain low-dimensional aspect to this problem. Above this, the acoustic spectrum falls away rapidly, as is to be expected since dominant unsteady features involve the trailing-edge and separation bubble dynamics, which we observe are predominantly intermediate-wavelength phenomena, between $\text{Im}\{\lambda\} \in [20, 60]$. Low-frequency dynamics, $\text{Im}\{\lambda\} < 20$, are largely absent from the spectrum. While very low-frequency phenomena, such as the low-frequency breathing of the separation bubble, typically with $\text{Im}\{\lambda\} < 1$ (see, for example, [12]), are expected to feature in the spectrum, these are observed to be acoustically silent at the measurement location. Furthermore, in the context of the spectrum shown in Fig. 3, this low-frequency region is resolved only by seven “bins,” and so much greater refinement of the frequency space is necessary to capture these modes.

Further potential for low-frequency system responses ($\text{Im}\{\lambda\} < 20$) exist through resonance pathways. Acoustic standing waves with wavelengths on the order of L_{upstream} or $L_{\text{downstream}}$ would be associated with plane waves with frequencies on the order of $\text{Im}\{\lambda\} = 2\pi n(Mu + a)/2L$, which leads to the fundamental mode being $\text{Im}\{\lambda\} \approx 1$. These are effectively suppressed by the sponge layers at both ends of the domain, that create essentially anechoic conditions. For modes propagating vertically, the maximum wavelength that can be sustained by the periodic system is therefore $L = 0.6$, for which the associated frequency is $\text{Im}\{\lambda\} = Mv + a/L \approx 10.5$. Doubling this gives $\text{Im}\{\lambda\} \approx 21$, but verification with the field for peak [0]⁵ shows that this is not a resonant structure.

The net result of this is that the peaks observed in Fig. 3 can be associated with amplified, self-excited instabilities rather than artifacts of the computational domain. Additionally, due to the laminar nature of this two-dimensional solution, the flow field lacks the transition to turbulence that characterizes the three-dimensional flow, and therefore the broadband component of the acoustics is missing here. However, in this paper we are concerned primarily with establishing the mechanics underlying the sensitivity analysis, and therefore we leave the extension to the fully physical, three-dimensional case for later work.

Extending this calculation of the FFT to every point within the domain, we isolate the fields for the observed peaks, which are plotted in Fig. 4. Here peaks [1] and [2] are associated with Kelvin-Helmholtz (KH) instabilities originating from the laminar separation bubble (to be characterized in Sec. III B) on the suction surface of the aerofoil, with the scattering of these coherent structures by the blunt trailing edge resulting in upstream-propagating acoustic waves. These two modes are also characterized by in- or out-of-phase dynamics, between the leading edge and the acoustic source at the trailing edge, for modes [1] and [2], respectively. Similarly, peak [5] is a higher-frequency shedding mode of the separation bubble, although the participation of the pressure surface, and the associated interactions at the trailing edge, now result in a downstream pressure field. Finally, the field for peak [7] illustrates the formation of a resonant structure forming within the blade passage. But rather than being excited by the previous KH modes, the pressure field shows high-amplitude fluctuations within the separated shear layer itself.

From these snapshots, it is clear that the flow is characterized by the interactions of the hydrodynamic and acoustic fields arising as a result of shear-layer instabilities interacting with the dynamics at the trailing edge. We therefore seek to establish the stability and sensitivity properties of these modes in single and multiple passages in the remainder of this paper.

B. Properties of the mean flow

Having confirmed the separation bubble and trailing edge dynamics as the key contributing sources to the acoustic spectrum, we briefly characterize these regions in the mean flow prior to our modal and nonmodal analyses in the subsequent sections of this paper.

⁵Here [★] corresponds to the labeled peak in the spectrum shown in Fig. 3.

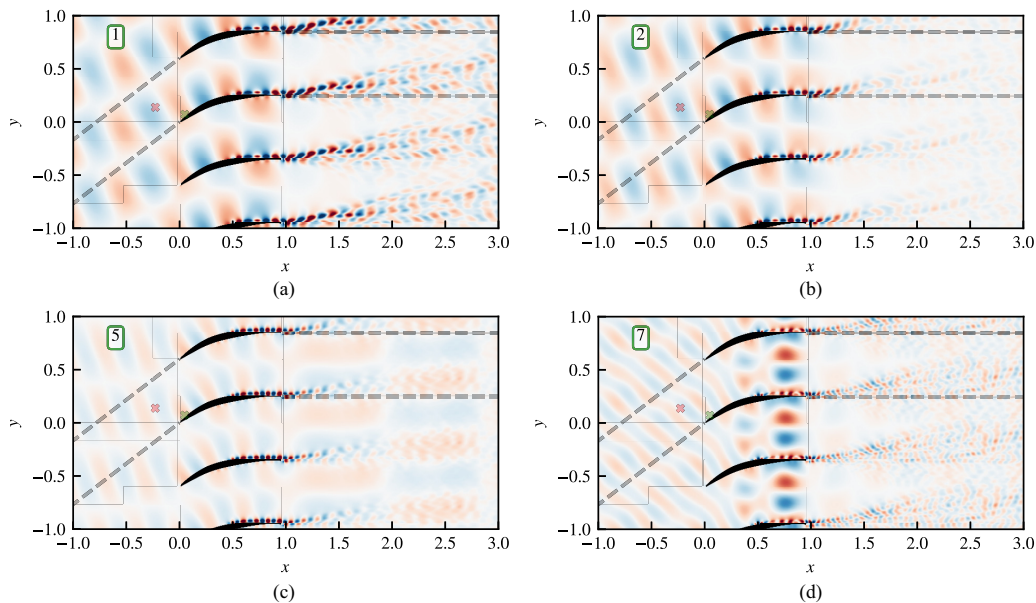


FIG. 4. The snapshots of the pressure fields corresponding to the main peaks identified in the Fourier transform of the nonlinear pressure field.

Inspecting Fig. 5(b), where we have parameterized the aerofoil surface as a function of arc-length, s , inflection points in the mean suction-side boundary-layer velocity profiles appear at $s \approx 0.35$ due to the adverse pressure gradient experienced by the flow at this point. Inflectional profiles are known to be a necessary condition for instability in the inviscid and incompressible limit, as shown by [55].

Further along at $s = 0.4$, the flow separates, as seen in the reversed flow in the velocity profiles in Fig. 5(b), and the streamlines of the separation bubble in Fig. 5(c), before reattaching at $s = 0.65$. Our observations of the bubble are in agreement with previous experimental [36] and three-dimensional laminar and turbulent numerical calculations [37,38]. Downstream of the reattachment point, the vortex shedding from the separation bubble leads to a thickening of the mean flow boundary layer. Although the velocity profiles here may suggest a propensity for the formation of convective instabilities in the flow, we should remember that the nonlinear flow is already highly unsteady, and we expect that this region of the mean flow serves more to support and amplify the instabilities that have grown downstream at the separation bubble, rather than modeling the growth of new instability mechanisms.

Fields along the pressure surface are similarly subject to adverse pressure gradients. However, the combination of the concave geometry and the flow conditions results in a flow that, although close to separating, remains attached at all points. This has two implications. First, the flow is again expected to be highly sensitive to flow disturbances, and, as will be seen later in Sec. III D, will participate in the global instability dynamics through receptivity mechanisms. Second, small changes in the flow conditions, such as alterations to the stagger angle, lead to separation on the pressure side, resulting in additional unsteadiness at the trailing edge as well as altered receptivity characteristics that dramatically change the acoustic signature of the aerofoil.

Finally, the mean velocity at the trailing edge, shown in Fig. 5(d), consists of a low-energy recirculating region immediately downstream of the trailing edge, with accelerated flow entering from the pressure side. The flow then entrains the lower-velocity, separated boundary layer from the suction surface downwards, with the resulting change in momentum deflecting the faster flow upwards, around one trailing-edge diameter downstream of the trailing edge. This change in

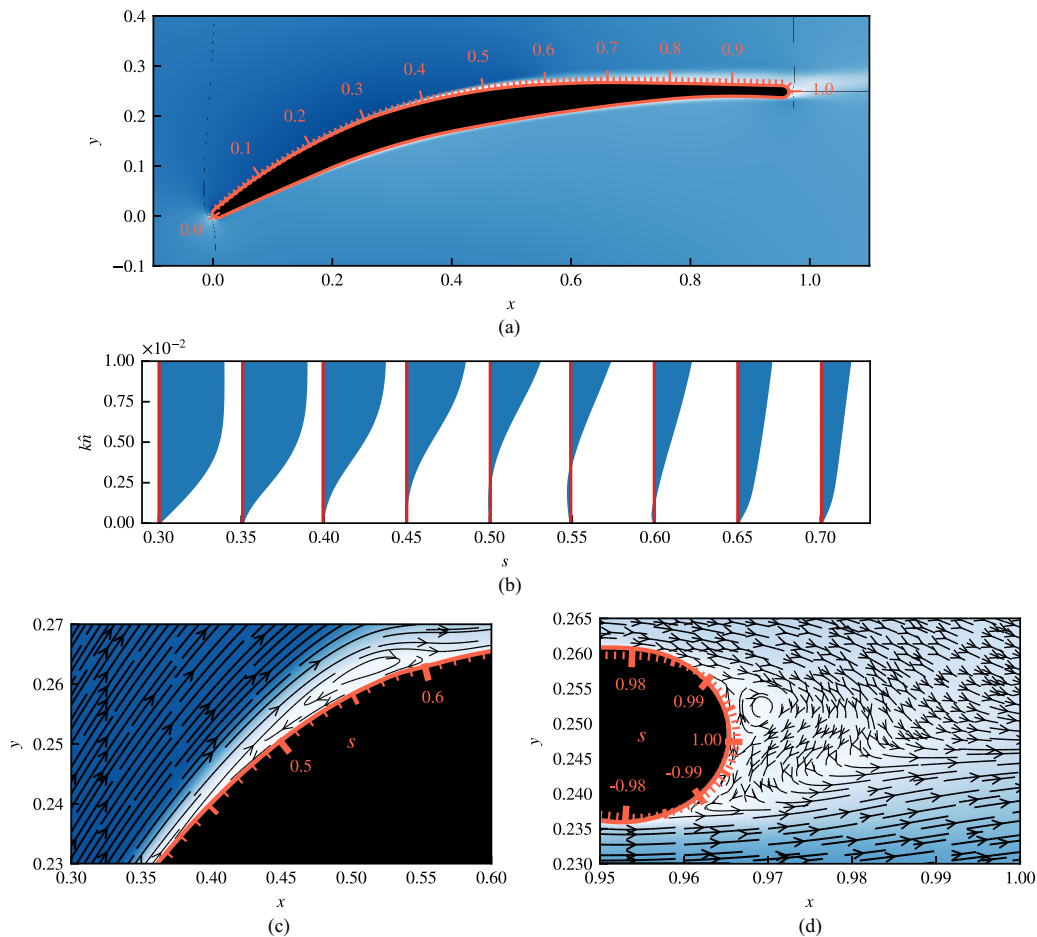


FIG. 5. The mean flow around the aerofoil showing (a) the absolute velocity field, $\|\mathbf{u}\|$ superimposed with an arc-length parametrization of the suction surface, and (b) the velocity profiles normal to the blade surface identifying the separation and reattachment points of the laminar separation bubble on the suction surface. Panels (c) and (d) visualize the local velocity field at the separation bubble and the trailing edge.

momentum may explain why the PS-SS vortex interaction at the trailing edge results in vortices being deflected upwards even though the flow remains axial in the far field. We should note that, while the mean flow does provide us with insights into the macroscopic features of the flow, in areas where the flow field is highly unsteady the computed field may never be attained physically at any point in the simulation. Furthermore, even though we have shown that the two-dimensional mean flow captures the key properties of the experimental mean flows, how these features carry on into the three-dimensional case should be the subject of a careful and detailed future study.

C. Impulse response analysis

We now turn our attention to the impulse response analysis of the linearized direct operator \mathbf{A} to analyze the transient growth phenomenon. It is an established fact that the linearized Navier-Stokes operator is nonnormal, and the corresponding nonorthogonality of the eigenvectors results in systems that may significantly amplify nonmodal perturbations over a finite time horizon, even in the presence of stable spectra [2]. A transient response analysis is therefore a prudent step, since not

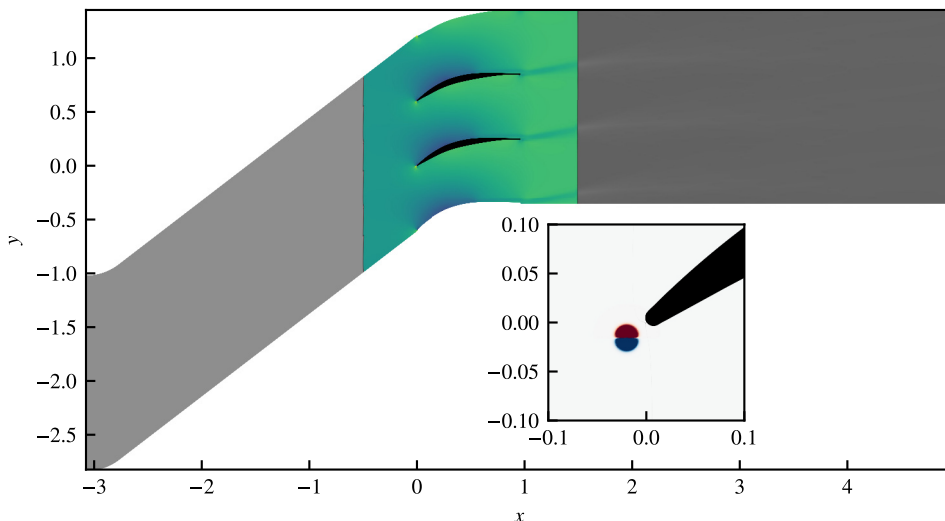


FIG. 6. The mean flow showing the active region of the seminorm in color. The region is taken over the whole height of the mesh and extends from $x = -0.5$ to $x = 1.5$. The inset axis shows the horizontal component of the velocity, u , for the initial linear disturbance.

only does it identify nonmodal amplification mechanisms that are absent from a modal perspective, but also identifies whether the global stability analysis of this system is an accurate description for the evolution of infinitesimal flow perturbations.

We consider the initial-value problem (IVP) given by Eq. (2), with $\mathbf{f} = \mathbf{0}$, and initial conditions $\mathbf{v}(t = 0) = \mathbf{v}_0$. The initial perturbation, with norm $\|\mathbf{v}_0\|_{\mathbf{M}} = 1$, takes the form of a divergence-free disturbance to the two velocity-field components. This is done so as to reduce the initial pressure transients, which would otherwise contaminate the linear field as they reflect within the blade passage and propagate through the periodic boundary in the upstream and downstream sections of the computational domain. The exact form of the perturbation is

$$p_0 = 0, \quad s_0 = 0, \quad u_0 = \frac{-2(y - y_0 - h_p \alpha)}{\sigma^2} e^{-r}, \quad v_0 = \frac{2(x - x_0)}{\sigma^2} e^{-r}, \quad (10)$$

with $\alpha \in \{-2, -1, 0, 1, 2\}$ to ensure that the initial condition is periodic, $\sigma = 5 \times 10^{-3}$ and

$$r = \frac{(x - x_0)^2 + (y - y_0 - h_p \alpha)^2}{\sigma^2}, \quad (11)$$

centered directly upstream of the leading edge at

$$(x_0, y_0) = (-0.02, -0.02 \tan(37.5\pi/180)). \quad (12)$$

In this way, the disturbance will be convected downstream and will interact with both the pressure and suction surfaces during the initial transient response. The mean flow, initial condition and the location of the seminorm used to measure the growth of this disturbance are shown in Fig. 6.

Equation (2) is integrated until $t = 20$ using an exponential Krylov time stepping algorithm, with snapshots saved at intervals of $\Delta t = 0.02$. Evaluating these snapshots and processing them using our seminorm gives the temporal evolution shown in Fig. 7.

From this, two main stages of the evolution may be identified. The first of these is the initial transient response, which we can define here to be between $t = 0$ and $t = 5$, which consists of transient growth, of one order of magnitude between $t = 0.4$ until $t = 0.75$, followed by an overall decay in the perturbation energy. Furthermore, for the first portion of this time window (until approximately $t = 2.5$) the evolution of the pressure and entropy components of the norm are

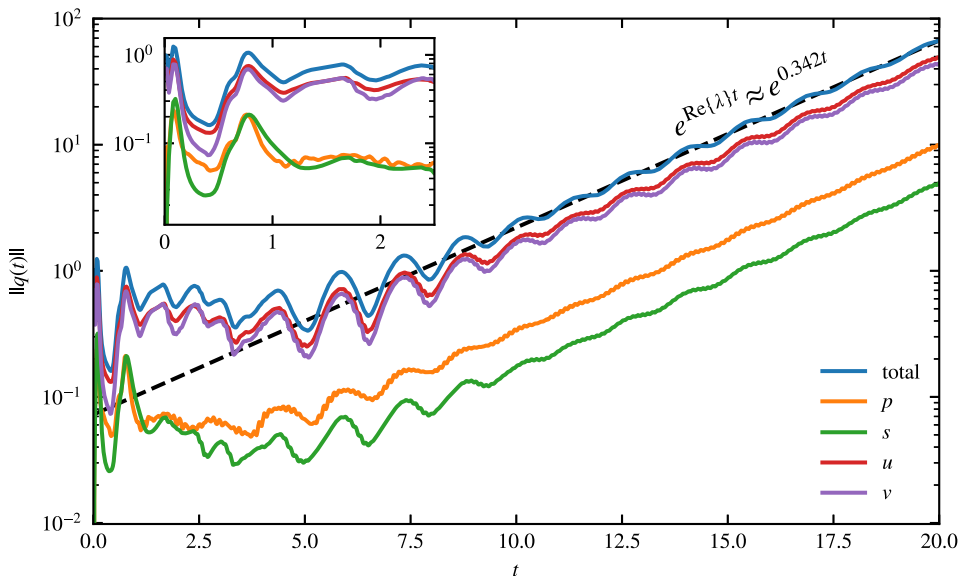


FIG. 7. Temporal evolution of the Chu seminorm for a divergence-free disturbance defined in Eq. (10). Contributions of the state vector components are also shown. The unstable asymptotic growth is indicated with a dashed line set to a growth rate of $\text{Re}\{\lambda\} = 0.342$.

closely correlated. This suggests that the system response is associated with the growth of boundary layer instabilities, without corresponding noise generation. Between $t = 2.5$ and $t = 5$ the pressure component increases, and acoustic radiation is observed from the trailing edge in the pressure field, but despite this increase in the pressure, the two velocity components and the entropy largely remain decaying. After $t = 5$ the system enters the phase of exponential growth punctuated by beating, where the system acts as an amplifier, and all components of the norm increase exponentially with the same growth rate of 0.342.

This breakdown into these two regimes not only highlights the nonnormality of the operator, which was touched on above, but also the presence of feedback mechanisms that drive and sustain the growth. In what follows, we will consider the two phases of evolution from a mechanistic perspective, and in the process we will attempt to identify the flow structures corresponding to features in Fig. 7.

1. Initial transients

Large-scale transient effects first appear when the perturbation interacts with the leading edge and the resulting energy is scattered as pressure waves from this region into the far-field, corresponding to the initial spike in the seminorm of Fig. 7 at $t \approx 0.1$. In Fig. 8 the remaining convective component of the disturbance subsequently splits into two vortices that are advected parallel to both boundary layers of the aerofoil. Behind these, wave packets of Tollmien-Schlichting (TS) type are formed through an energy transfer from the vortices to the boundary layers. Note that between $t = 0.1$ and approximately $t = 0.4$ the system remains dissipative, and while the pressure-side TS wave packet can be seen to grow, the suction side packet is highly damped as a result of the favorable pressure gradients at that point.

The dynamics of the norm change, once the wave packet reaches the separation point of the separation bubble, and enters the detached shear layer. Kelvin-Helmholtz instabilities amplify the incoming disturbance here, with the amplified features sustained until they are convected past the trailing edge, at which point they are scattered as pressure waves into the free stream.

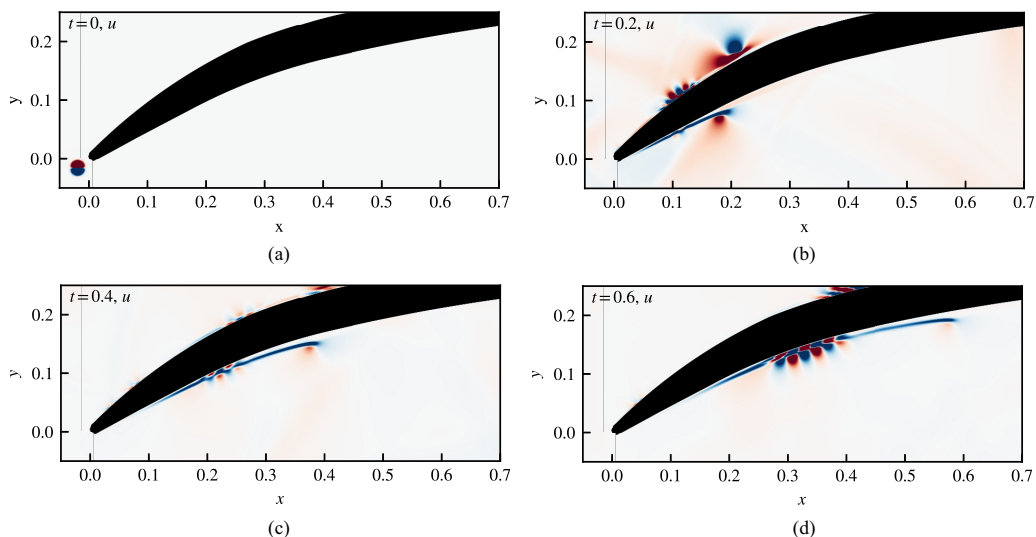


FIG. 8. Plots of the streamwise velocity component u showing the initial transient responses in the vicinity of the leading edge. (a) $t = 0$, (b) $t = 0.2$, (c) $t = 0.4$, and (d) $t = 0.6$.

Meanwhile, within the separation bubble, tilted structures reminiscent of those of the Orr mechanism are observed (see Fig. 9).

2. Establishing the feedback mechanism

Returning back to the pressure waves scattered at the trailing edge, we note that the acoustic waves are propagated predominantly upstream, as seen in the earlier nonlinear solution. This exposes the boundary layers to periodic forcing arising from the unsteady interactions between the unstable shear layer, and in the process visibly generating TS waves on the pressure surface in Fig. 10. These waves propagate downstream before arriving at the trailing edge to be scattered into acoustic waves.

A similar receptivity mechanism is also observed upstream of the separation bubble in Fig. 10. The process here is different to the one on the pressure side, however, since after the waves are generated, they are amplified by the separation bubble before propagating downstream, in a manner similar to that observed with the Orr mechanism in the section above. These amplified structures are then convected downstream, and sustained by the detached shear layer before once again scattering at the blunt trailing edge. It appears that this extraction of energy from the mean flow to the

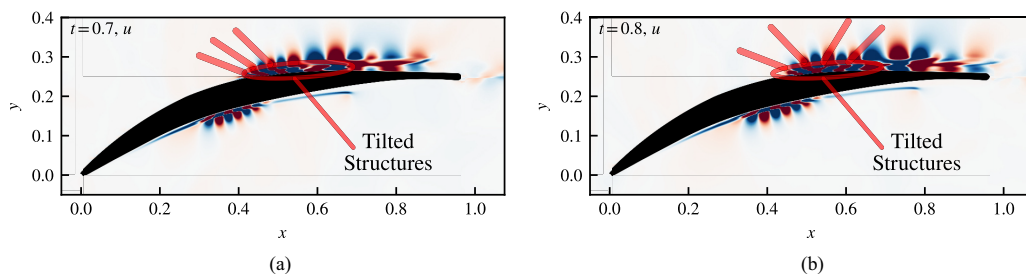


FIG. 9. Plots of the streamwise velocity component u showing tilted structures reminiscent of the Orr mechanism highlighted on the suction surface of the aerofoil. (a) $t = 0.7$ and (b) $t = 0.8$.

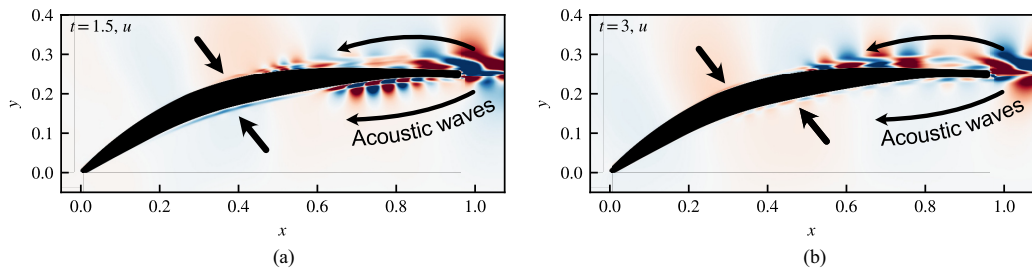


FIG. 10. Plots of the streamwise velocity component u indicating the receptivity to acoustic forcing of the upstream boundary layers on the pressure and suction surfaces, leading to the formation of TS waves. Note the acoustic waves are less visible here since the u field is plotted to highlight the hydrodynamic wave packets. (a) $t = 1.5$ and (b) $t = 3.0$.

perturbation through this feedback mechanism is the driver of the exponential growth seen in the latter part of Fig. 7.

Amplification of structures on the pressure and suction surfaces is shown in Fig. 11, using the entropy field to isolate the convective features. At the suction surface the reattachment of the flow between $s = 0.60$ and $s = 0.65$ demonstrates amplification by a factor of $k = 5.21$, compared to the amplification of $k = 5.07$ between $s = 0.37$ and $s = 0.60$. As a result, the processes within the separation bubble act as efficient amplifiers, with an overall growth factor of $k = 26.45$ between the origin point of the instability and the eventual structure that is convected past the trailing edge, although nonlinear processes likely regulate this growth rate in the fully nonlinear flow. Following our observation in Fig. 10, waves are similarly seen on the pressure side, although maximum amplification of the flow now occurs in the vicinity of the midchord, with the probe at $s = -0.56$ recording a growth rate of $k = 2.55$ against the signal at $s = -0.37$. These waves then decay, and so the relative growth rate between $s = -0.37$ and $s = -0.76$ is only $k = 1.33$. In the future, a further resolvent analysis could be performed here to determine the transfer functions governing the growth rates of harmonic disturbances introduced within the boundary layers.

3. Asymptotic behavior

From approximately $t = 5$ until the end of the simulation, the system enters a period of unbounded exponential growth, punctuated by a beating phenomenon occurring at time scales on the order of the convection time for structures on both blade surfaces, which is also seen with the formation of wave packets in Fig. 11. Having identified the asymptotic growth rate in Fig. 7 as $\text{Re}\{\lambda\} \approx 0.342$, we form $\|\mathbf{q}(t)\| \exp -\text{Re}\{\lambda\}t$ to obtain Fig. 12. From this the beating is clearly seen as a modulation of the pressure signal, with a time period of $\Delta t = 1.42$, with an expected frequency gap of $\Delta\lambda_i = 2\pi/\Delta t \approx 4.43$ between two unstable modes.

Axial velocity fields, given in Fig. 13 for the respective “falling” ($t = 6.0$) and “rising” ($t = 6.5$) parts of the norm. These show that the flow alternates between states of highly amplified hydrodynamic features on the suction side, with low levels of acoustic radiation, and states of high acoustic excitation when these features reach the trailing edge and are scattered.⁶

⁶The times of the snapshots are not the local maximum and minimum of the norm oscillation, as seen in Fig. 12, because we want to visualize the modulation of the convective structures on the suction surface, and there is a time lag between the formation of the structure and the response of the acoustic source registered in the norm.

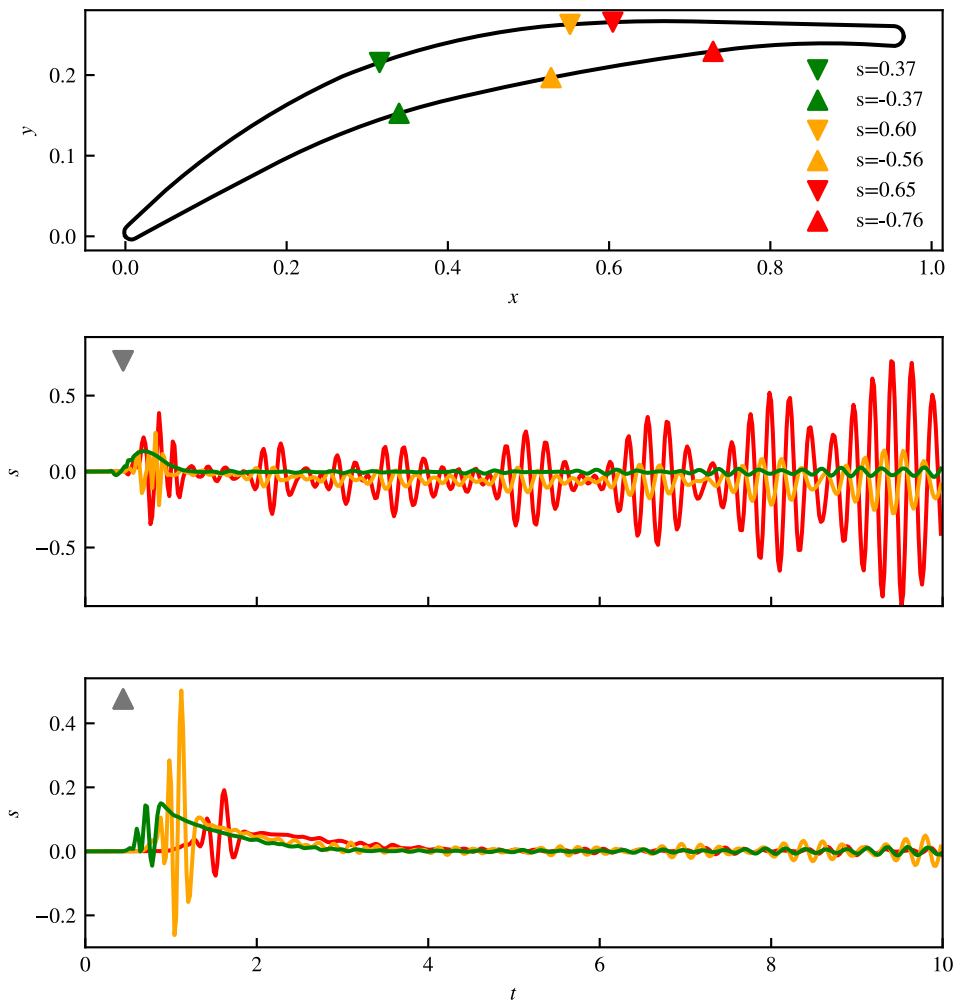


FIG. 11. The amplification of disturbances within the pressure-side and suction-side boundary layers for the time interval $t = 0 \rightarrow 10$, as illustrated by the entropy signal at the locations shown in the uppermost panel. Locations on the suction surface are indicated by the “inverted” triangles and the entropy traces shown in the second graph, while the locations on the pressure surface are shown with “upright” triangles and the results shown in the lower panel.

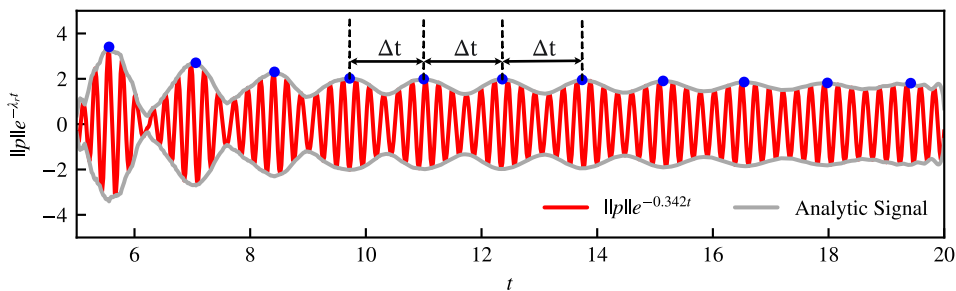


FIG. 12. Asymptotic evolution of the pressure component of the seminorm, showing the signal as well as the amplitude envelope function. The average peak spacing is $\Delta t = 1.42$.

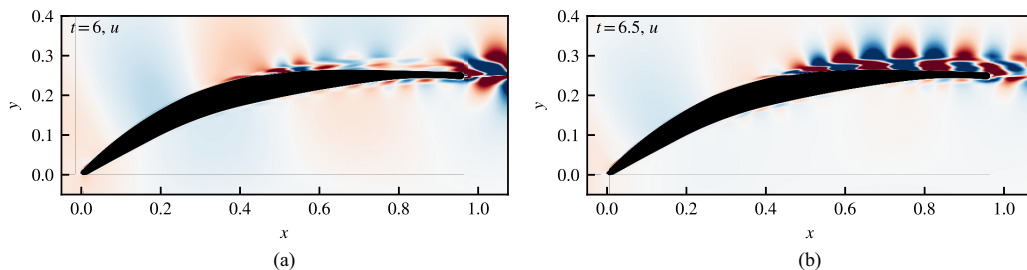


FIG. 13. The “beating” phenomenon observed primarily on the suction side as the system enters the final phase of exponential growth. Note the stronger acoustic shedding at (a) $t = 6$ and the amplified hydrodynamic features on the suction surface at (b) $t = 6.5$.

4. Comparison to prior work

Similar⁷ impulse-response observations have also been made for isolated CD aerofoils [31], where a 5° -angle-of-attack case produced a spanwise-homogeneous mode that exhibited a rapid decay in magnitude followed by a sustained growth alongside a beating. This was attributed to the presence of aeroacoustic feedback mechanisms. The upstream-biased directivity of the acoustic source at the trailing edge was also noted to be similar to the observations in this section, although there also appears to be an absence of sustained hydrodynamic instabilities on the pressure surface, unlike what is observed here. An increase of the angle of attack to 8° was shown to stabilize the impulse response. This is attributed to the removal of the laminar separation bubble located near the trailing edge on the suction side, and instead increasing the size of the reattaching separation bubble near the suction-side leading edge, which, in nonlinear simulations, subsequently transitions to turbulence along a large portion of the suction surface.

Impulse stability analyses of this kind are exceedingly rare for cascade configurations, however, with one of the few being an analysis of a single-passage high-pressure turbine (HPT) cascade [56]. This analysis specifically considered trailing-edge blowing as a means to control the trailing-edge source, by reducing the maximum velocity in the recirculation region downstream of the trailing edge. Much like this study, the case with no trailing edge blowing exhibits a decay followed by an exponential growth of the disturbance, punctuated by beating. The mode that is spanwise homogeneous also exhibits the highest growth rates. As the trailing-edge blowing is increased, the system first transitions to a damped oscillatory mode and subsequently to a fully damped response, where the disturbance decays exponentially. The conclusions drawn by the authors included a hypothesis that the suppression of the acoustic source is associated with the removal of the recirculation region at the trailing edge; however, this disagrees with the CD-aerofoil calculations [31], where the presence of the laminar separation bubble was observed to be the primary factor in determining the aeroacoustic feedback loops. This case is also interesting from the point of view of the present study because the HPT cascade contains shocks that prevent the propagation of the acoustic waves upstream. Instead, the interaction between the blades is facilitated by the propagation of waves from the trailing-edge source to the suction-side boundary layer of the blade below. Therefore, unlike our study, the interaction here is exclusively unidirectional, although the limitation to a single passage restricts the observation of potential macroscopic behaviours that might exist here. By comparison, it will be shown in part II [32], which relaxes the restriction of this analysis to a single passage, that the subsonic linear CD cascade presented here exhibits feedback mechanisms that allow for disturbances to propagate both upwards *and* downwards along the axis of the cascade.

⁷These impulse response analyses are conducted using the forced Navier-Stokes approach rather than using a consistent linear-operator analysis, as is done here.

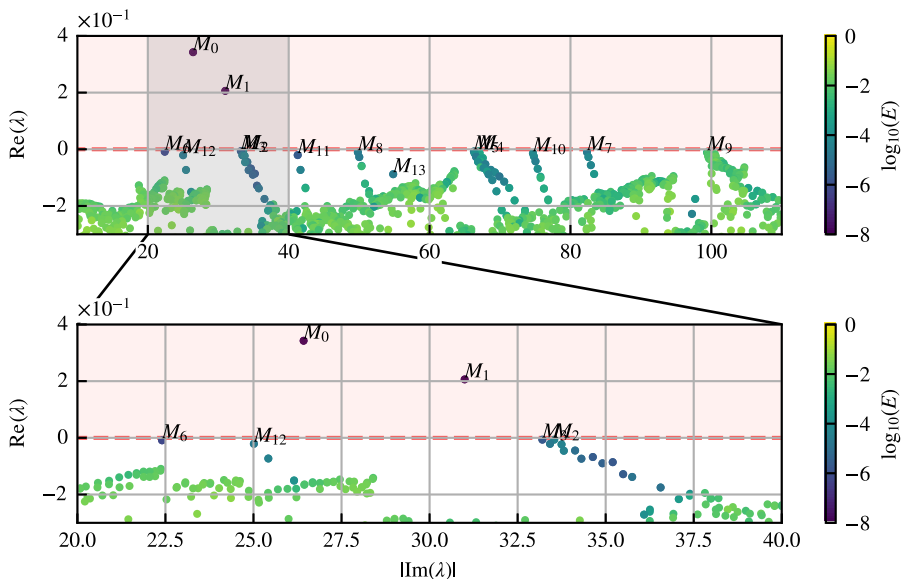


FIG. 14. The direct global modes of the linear operator \mathbf{A} with respect to the mean flow, with the inset region below showing a magnified portion of the spectrum for $D_f = \{\lambda : \text{Im}\{\lambda\} \in [20, 40]\}$. The eigenvalues are colored by the L_2 relative error of the eigenvalue-eigenvector pair with respect to the time-stepping operator (see discussion). The 14 most unstable modes in D_f are labeled $M_0 \rightarrow M_{13}$.

D. Operator spectrum

The spectrum of the direct operator \mathbf{A} is shown in Fig. 14. As expected from our earlier analysis of the impulse response in Sec. III C, this spectrum is globally unstable with respect to the mean flow. It consists of two eigenvalues in the unstable half-plane, corresponding to Kelvin-Helmholtz modes on the suction surface, as well as a collection of marginally stable modes with nonzero frequencies. For some of these marginally stable modes, the mode is present in association with branchlike structures that are more heavily damped than the “root” mode located on $\text{Re}\{\lambda\} = 0$, with the angle of the branch (i.e., frequency shift of the mode with respect to the damping) corresponding to the physical location within the domain where the dynamics of the mode are represented. This suggests [39] that this phenomenon arises as a result of weak resonance structures between the blade and the domain boundaries.⁸ Note also that we have removed the modes with zero frequencies here since these are poorly converged as a result of the time-stepping method used to compute the spectrum. For the purpose of this work, however, this is not a significant concern, since our goal here is to identify the key mechanisms responsible for the dominant features present in Fig. 3, which are seen predominantly for $\text{Im}\{\lambda\} \in [20, 90]$.

Temporal frequencies of the modes, and the relative errors between the modes and the frequencies identified in the FFT (see Fig. 3) are calculated. The dominant peak in the FFT corresponds to mode M_1 , with a relative frequency error of 1.82%, while modes M_0 , M_2 , and M_3 all have errors below 3%. Note, however, that the most unstable mode, M_0 , does not correspond to the dominant peak in the FFT, suggesting that important nonlinear effects, that are not captured by a modal analysis, play a role in selecting the frequency.

⁸In other words, if the acoustic component of the mode is located predominantly in the downstream, the branch is shallower with respect to the real axis as a result of the lower velocity of the mean flow in that region.

TABLE II. Eigenvalues of the selected modes. Modes attributable to peaks identified in the FFT are compared to the FFT results in Fig. 3, and relative errors are given.

Mode	Eigenvalue	FFT frequency	$\Delta\text{Im}\{\lambda\}$	FFT peak index
M_0	$0.3426 + 26.4230i$	27.17	2.75%	[1]
M_1	$0.2061 + 30.9954i$	31.57	1.82%	[2]
M_2	$-0.0063 + 33.5399i$	33.30	0.72%	[3]
M_3	$-0.0064 + 33.2027i$	33.30	0.29%	[3]
M_4	$-0.0069 + 66.9689i$			
M_5	$-0.0075 + 66.2931i$			
M_6	$-0.0087 + 22.4041i$	20.73	8.08%	[0]
M_7	$-0.0104 + 82.3487i$			
M_8	$-0.0105 + 49.8186i$			
M_9	$-0.0108 + 99.4057i$			
M_{10}	$-0.0143 + 74.6719i$			
M_{11}	$-0.0205 + 41.2794i$			
M_{12}	$-0.0211 + 25.0113i$			
M_{13}	$-0.0880 + 54.8335i$			

E. Structural, sensitivity, and receptivity analysis

Having obtained the operator spectrum in the previous section, we are now in a position to analyze the structures within the eigenvectors. To do so, we restrict ourselves to modes in $|\text{Im}\{\lambda\}| \in [20, 90]$, and, using the representative modes M_i , we are able to identify three main categories of modes. These are (1) modes describing the coupling effects arising from the scattering of unsteady features from the suction side at the trailing edge, (2) unamplified high-frequency modes from the unsteady shear layer of the separation bubble, and (3) trapped modes demonstrating the possibility of self-excited resonance.

1. Dominant modes: Bubble-TE coupling

a. Dominant structures. Modes M_0 , M_1 , M_6 , and M_{12} represent the most dominant structures of this system and correspond to the largest peaks in the FFT of the upstream pressure field, as established in Table II.

Figure 15 shows the normalized pressure and axial velocity for these modes. It is clear from this figure that the modes all share a dipole-like structure at the trailing edge which propagates acoustic waves upstream through the passage and into the far field, with minimal acoustic propagation downstream of the trailing edge. Instantaneous surface pressure distributions of these fields suggest that the modes being selected are those that are able to support small-fraction rational axial wavelengths, ranging from in-phase dynamics on each surface in M_{12} to M_0 supporting two wavelengths on its suction side and $3/2$ wavelengths on the pressure side, for example. The wake regions for all these cases are correspondingly similar, at least up to the spatial wave numbers of the structures. What is clear, however, is the participation of the suction-side instability in these dynamics, with the appearance of the convective structures, suggestive once again of an upstream receptivity mechanism. This coupling appears to be strongest for M_0 and M_1 , while M_6 and M_{12} have lower pressure and velocity amplitudes on the suction surface, proposing that the dynamics of these modes are related more to trailing edge processes than to the amplification at the separation bubble. This is borne out in Fig. 16, where the pressure traces confirm that the pressure distributions on the suction surface for the latter modes are amplified further downstream compared to the more unstable structures, which experience the main amplification at the separation bubble.

Interestingly, the amplification of M_1 in both the p and u fields is 1.31 and 1.59 times larger, respectively, than for M_0 , and occurs marginally earlier on the suction surface for the latter mode,

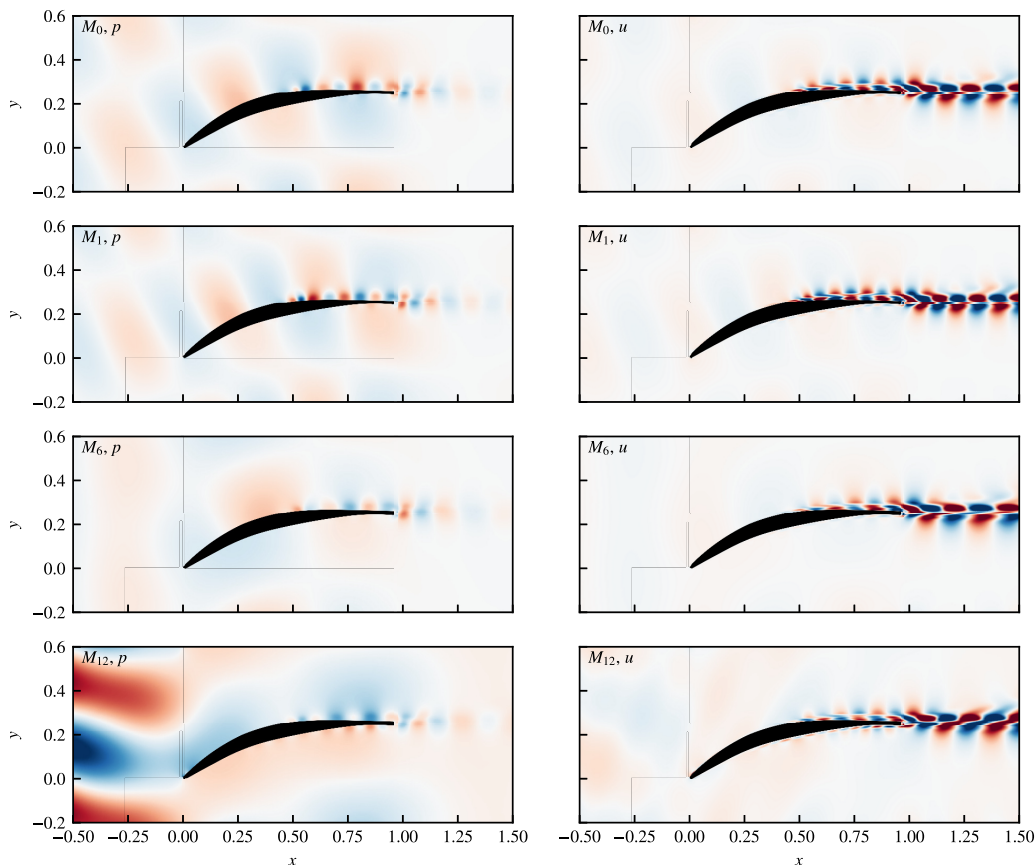


FIG. 15. The real part of the pressure and axial velocity for the modes M_0 , M_1 , M_6 , and M_{12} normalized with respect to the near-wake maximum axial velocity.

but decays to a level smaller than M_0 on both surfaces by the time it reaches the trailing edge. Also, the near-wall flow on both the pressure and suction sides consists of a superposition of the vortex dynamics and the upstream-propagating acoustics field, leading to nodes and antinodes in the pressure field. The higher frequency (both spatial and temporal) of M_1 may result in a node that is located further upstream on the laminar separation bubble when compared to M_0 . This may be the mechanism through which M_1 is selected in the nonlinear field as the dominant acoustic source, although a careful nonlinear analysis is required to determine this, which is outside the scope of this study.

Pressure-side traces show that pressure signals are amplified in $x > 0.5$ for all modes except M_6 , with M_{12} also experiencing amplification in the region $x \in [0.1, 0.35]$, which is unlike the other modes of this family. Spatial growth rates for M_0 and M_1 differ most following the onset of the instability for $x \in [0.2, 0.4]$, where the pressure amplitudes of M_1 are below those of M_0 . However, the M_1 mode is strongly amplified from $x = 0.35$, attaining $|p| = 0.013$ although this growth is not reflected in the amplitudes of the axial velocity u , for which all modes (except M_{12}) have comparable amplitudes of $|u| \approx 0.026$.

b. Downstream modes. This Kelvin-Helmholtz instability is also responsible for the modes M_2 and M_3 that result in downstream propagating waves, as shown in Fig. 17. The differences between these modes and the ones in Fig. 15 appear to be the modification of the trailing edge shedding, with a high-pressure zone originating from the suction surface that is unmatched by a similar strength feature originating from the pressure side.

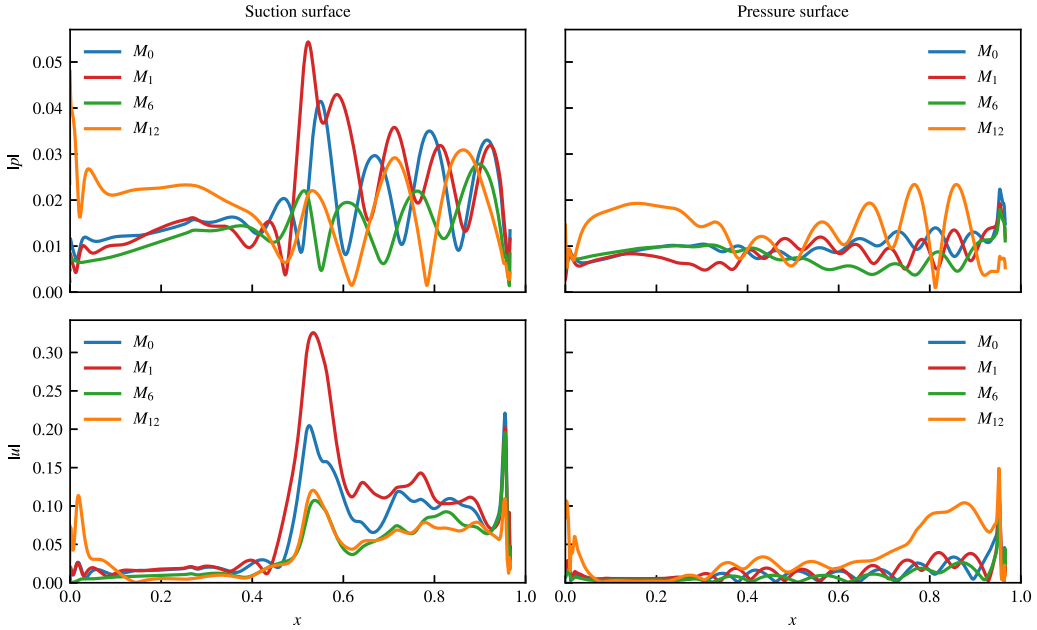


FIG. 16. Surface pressure and velocity dynamics for the modes M_0 , M_1 , M_6 , and M_{12} .

Analysis of blade-surface pressure and velocity traces (not shown here) show peak pressure amplitudes on the suction surface of $\|p\| = 0.055$, which is equivalent to the maximum amplitude attained by M_1 , and similarly $\|p\| = 0.024$ on the pressure surface: double that of M_1 . However, pressure-side velocity amplitudes for $M_{2/3}$ have only a maximum of $\|u\| = 0.022$ compared to M_1 , where the amplitude is $\|u\| = 0.032$. This indicates that, despite the additional forcing of the boundary layer on the pressure surface, the response of this boundary layer is diminished, which leads to this modification of the shedding at the trailing edge.

c. Adjoints and wavemakers. Adjoint structures corresponding to the dominant modes are shown for the streamwise velocity component in Fig. 18(a), where they are normalized so that $\langle \mathbf{w}, \mathbf{v} \rangle_{\mathbf{M}} = 1$.

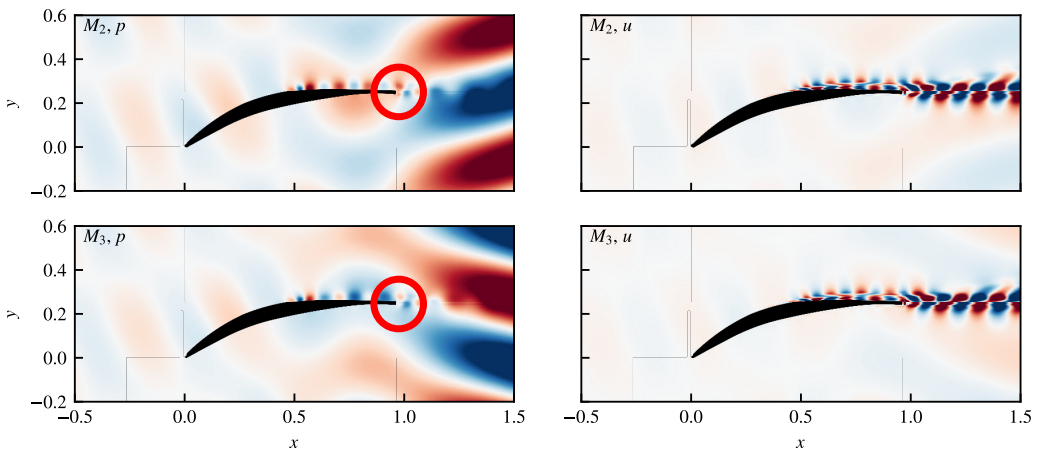


FIG. 17. The direct pressure component of M_2 , M_3 , the downstream modes. The red circles indicate a modification of the vortex shedding at the trailing edge.

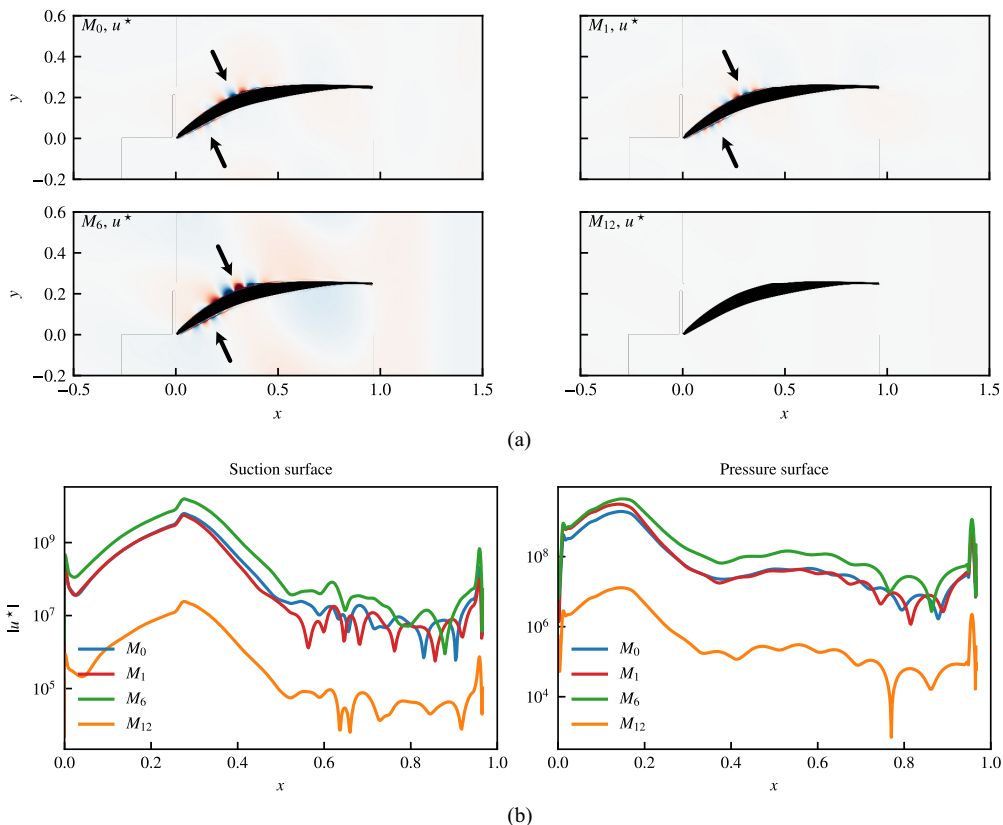


FIG. 18. The adjoint horizontal velocity field of M_0 , M_1 , M_6 , and M_{12} in (a), with the surface traces in (b).

These show that M_0 , M_1 , M_6 , and M_{12} have compact supports for sensitivities in regions upstream of the separation bubble as well as, on the pressure surface, in the vicinity of the leading edge with peak sensitivities attained at $x = 0.277$ and $x = 0.122$ on the suction and pressure sides, respectively. This is based on the adjoint traces at the blade surface in Fig. 18(b). M_6 is found to be the most sensitive of the modes, with M_{12} the least, which may help to explain why M_{12} does not appear as a peak in Fig. 3. M_0 and M_1 have similar sensitivities, except for a (maximum) 13% relative increase (attained at $x = 0.30$) in the sensitivity of M_0 relative to M_1 downstream of the separation point on the suction side.

Before advancing this discussion, we first present the wavemaker regions that locate the origin of the instability characterizing the mode. Figure 19 shows that the wavemakers for M_0 , M_1 , M_6 , and M_{12} share similar supports along both surfaces of the aerofoil: the overarching pattern here being regions of sensitivity upstream of the laminar bubble on the suction surface and, perhaps more surprisingly, a smaller, though similarly significant, region of sensitivity close to the leading edge on the pressure side. Numerical simulations performed earlier for the self-noise problem on isolated NACA-0012 aerofoils [13] have shown similar receptivity properties on both surfaces of the isolated aerofoil, with the conclusion being made that, since the two surfaces are not *convectively linked*,⁹ this constitutes as direct evidence of the receptivity of the associated boundary layers to upstream-propagating acoustic waves. Indeed we have seen in the impulse response, and from the modes in

⁹In other words, there is no pathway of purely convective structures forming on one of the surfaces to interact at later times with the other surface without being scattered into acoustic waves.

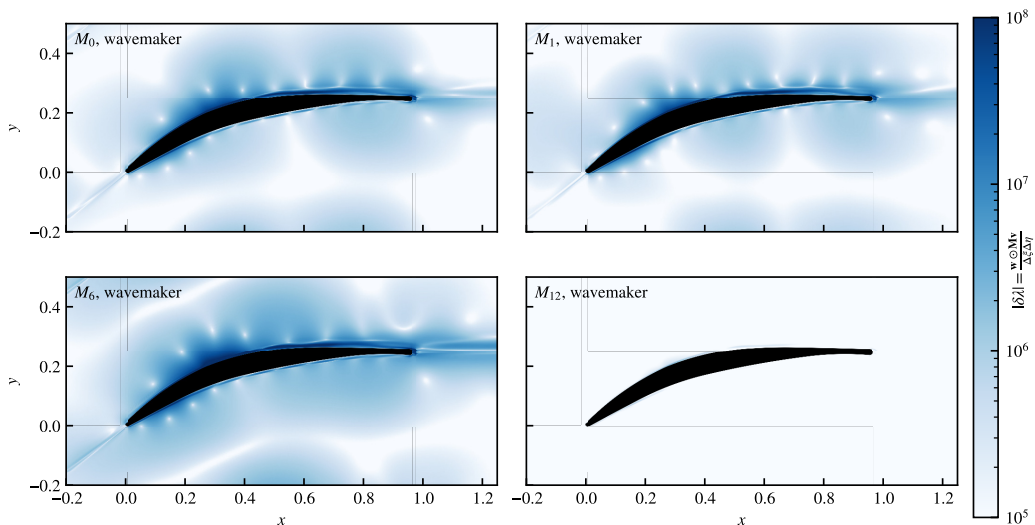

 FIG. 19. The wavemakers for M_0 , M_1 , M_6 , and M_{12} .

Fig. 15, that these two regions are responsible for the generation of the Tollmien-Schlichting waves that are amplified and convected down to the trailing edge.

Application of control strategies for suppressing these dynamics would be most effective in these wavemaker regions, and would result in the greatest change to the eigenvalue with the least amount of control effort.

Unlike the earlier numerical experiments on isolated aerofoils, however, the pathways for the interaction are more complex in the cascade configuration. The scattered acoustic waves are now not only interacting with the blade through an upstream propagation, but also through interactions between the suction side of the dipole and the pressure-side boundary layer and vice versa. What is more, the acoustic waves can also be scattered by the leading edge and redirected onto the pressure or suction surfaces. This introduces additional coupling effects, although we will postpone this analysis until Part II, where the extra degrees of freedom from the N -periodic blade row will make these processes clearer.

c. Relationship to the impulse response. It is instructive to recall that the superposition of two sinusoidal waves can be written as

$$\cos(\text{Im}\{\lambda_0\}t) + \cos(\text{Im}\{\lambda_1\}t) \quad (13)$$

$$= 2 \cos\left(\frac{\text{Im}\{\lambda_0\} + \text{Im}\{\lambda_1\}}{2}t\right) \cos\left(\frac{\text{Im}\{\lambda_0\} - \text{Im}\{\lambda_1\}}{2}t\right), \quad (14)$$

with the envelope function taking the form

$$f_{\text{envelope}} = 2 \cos\left(\frac{\Delta\text{Im}\{\lambda\}}{2}t\right). \quad (15)$$

Though the pairwise frequency difference between many of the modes in Fig. 14 is similar, only M_0 and M_1 are nondecaying and thus are the only ones able to sustain the beating for $t > 15$. From Table II, $\Delta\text{Im}\{\lambda\} \approx 4.43$, which matches the difference in frequencies of M_0 and M_1 : $\Delta\text{Im}\{\lambda\} \approx 4.57$.

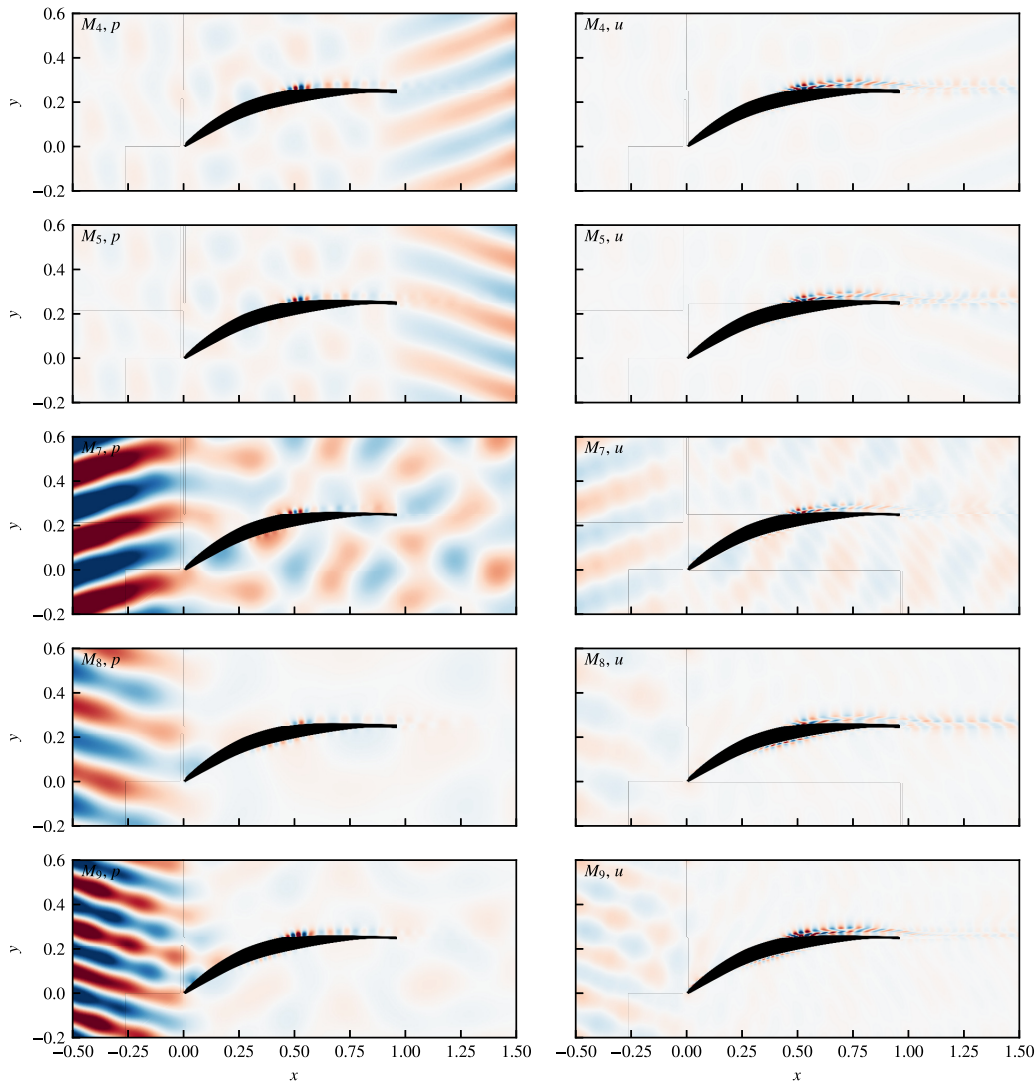


FIG. 20. The high-frequency direct modes associated with shear layer instabilities at the separation bubble.

2. High-frequency modes: Bubble dynamics

In addition to the dynamics examined above, the direct model similarly identifies high-frequency ($\text{Im}\{\lambda\} > 50$) structures associated with the shearing on the surface of the laminar bubble. These modes are M_4 , M_5 , M_7 , M_8 , and M_9 , and are shown in Fig. 20.

The hydrodynamics of these modes are confined primarily to the free shear layer of the separation bubble, with a peak for all modes at $x = 0.51$. The structures downstream have negative growth rates, resulting in minimal interactions with the trailing edge, as evidenced by the u plots in Fig. 20. Furthermore, the amplified structure on the separation bubble is approximately three wavelengths in size before decaying in the streamwise direction. Despite this, the acoustic source nevertheless produces waves in the downstream region, for M_4 and M_5 , and in the upstream region for M_7 , M_8 , and M_9 . The relationship between these two groups appears to be the inclusion of pressure-side structures in the latter group, with amplified wave packets persisting between $x = 0.25$ and $x = 0.6$, as seen in Fig. 21. The adjoint field (not shown) is sensitive once again at the separation point

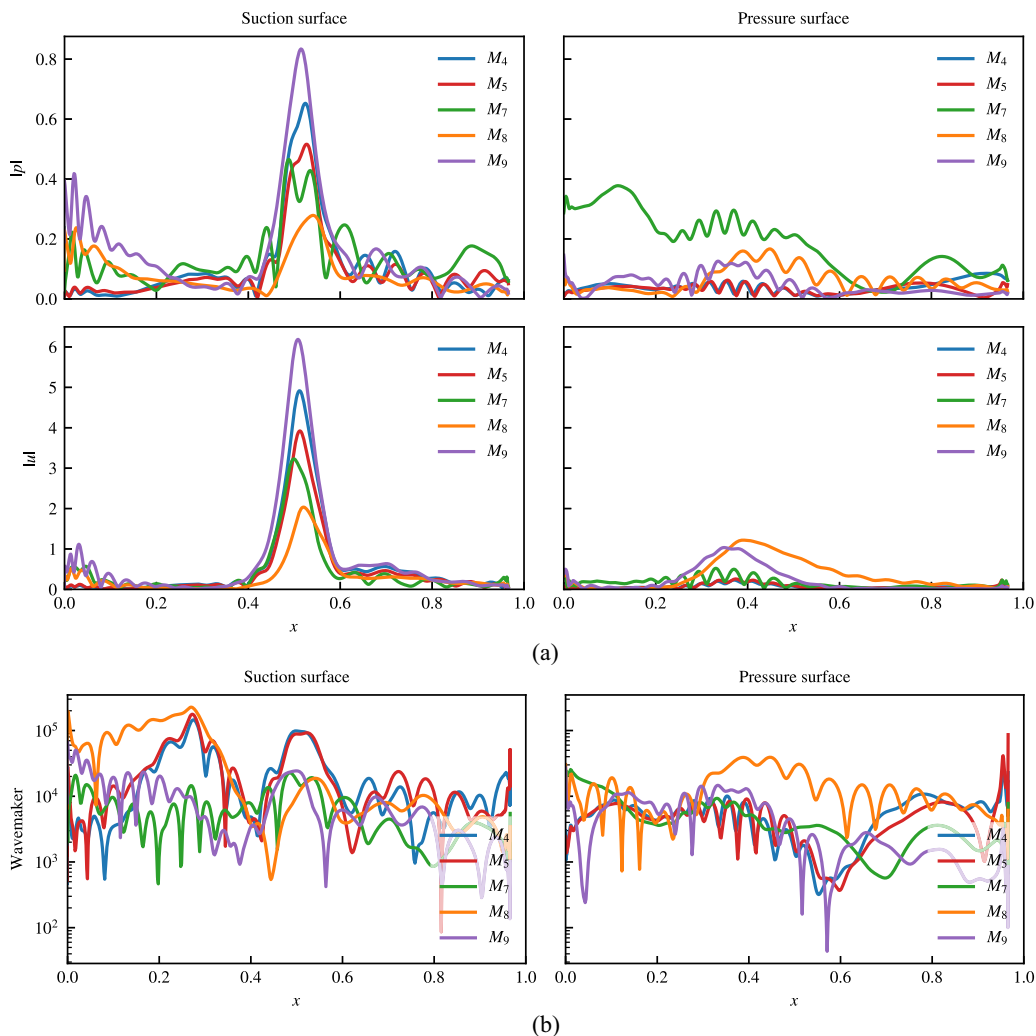


FIG. 21. The surface traces of the high-frequency modes for the (a) direct modes and (b) the wavemakers.

at $x = 0.30$, although now the direct mode is concentrated at $x = 0.51$. Hence the wavemaker in Fig. 21(b) is now three orders of magnitude smaller than the wavemakers calculated for the dominant modes, suggesting that these modes amount to robust instabilities that are intrinsic to the flow.

3. Confined modes

The final category of modes that have acoustic structures that are suggestive of acoustic resonances within the blade passage are shown in Fig. 22, alongside the adjoint and wavemaker surface pressure traces. Though these modes are not trapped in the sense that they still “leak” acoustic energy into the upstream far field, their structures contain regions of intensified pressure that are nonetheless confined between the two aerofoil surfaces. Similar effects have been observed in both experimental [57] and in industrial settings (see review in [58]), especially in multistage compressors, and are highly sensitive to the particular flow conditions.

Although we will not be performing a parametric flow analysis for this case, we nevertheless note that the form of the resonance in M_{11} and M_{13} are confined to a pitchwise orientation near the trailing edge, and between the separation bubble, and near the leading edge on the pressure side in the case

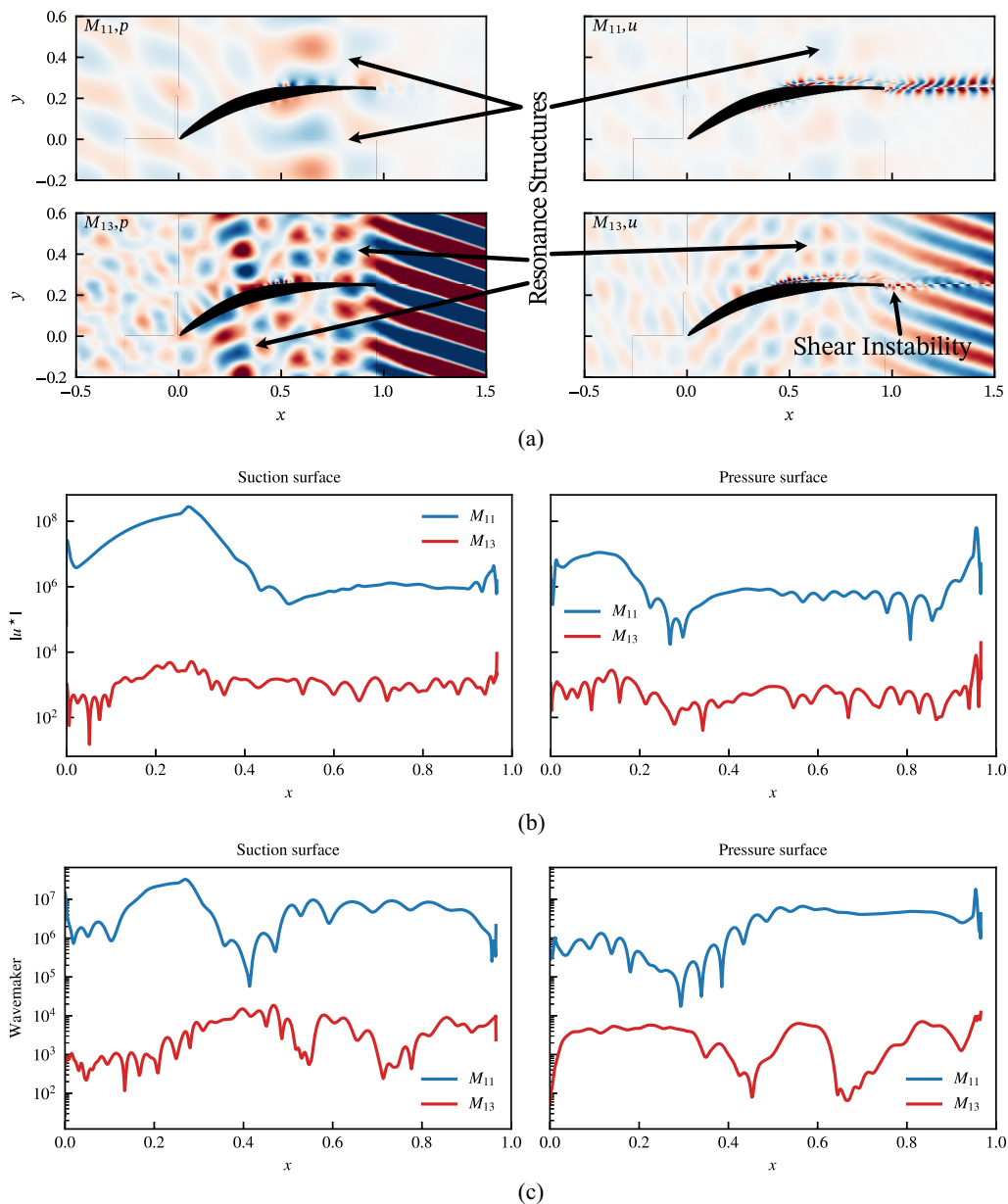


FIG. 22. The modes M_{11} and M_{13} show confined features between the pressure and suction surfaces. The direct fields are shown in (a), with adjoint surface traces in (b) and wavemakers in (c).

of the former. On the other hand, from Fig. 22, M_{13} does not appear to be triggering any instabilities on the pressure-side boundary layer and is otherwise insensitive, especially when compared to M_{11} , which is confirmed by the wavemakers in Fig. 22(c). This suggests that the mechanism behind the structures described in *this particular case* is a combination of directivities of the acoustic source aligning with acoustic rays that are perpendicular, or at least close to perpendicular, to both aerofoil surfaces—and this combination traps a portion of the acoustic energy inside the blade passage

As a final observation in this section, note that unlike virtually all other modes considered previously which exhibited either localized structures or had a coupling between the unsteadiness

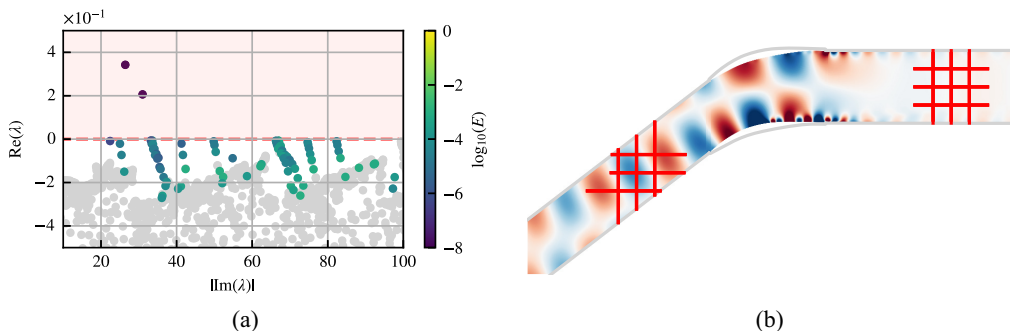


FIG. 23. To the left, the modes selected for the phase and group velocity analysis are shown in color while the rejected modes are represented as grey points. To the right, the interpolation contours along which the wave number is computed. The middle vertical contour is placed at $x_c = -1$ in the upstream and $x_c = 2$ in the downstream, with the neighboring contours placed either side at $x_{\pm} = x_c \pm 0.15$, and extend to the full height of the passage. The horizontal contours are similarly equispaced in y , with y_c , the central contour, placed at the midpoint of the central vertical contour. The total length of these is fixed at 0.6 and the midpoint adjusted so that the entire contour fits into the single-passage flow domain.

at the blade surfaces and the full wakes, M_{13} exhibits localized effects in the near wake, and is confined to instability waves within the separated shear layer that was identified at the trailing edge in Sec. III B.

The relationship between the dominant linear direct modes and the FFT analysis of the nonlinear field is clear to see, even through a cursory examination of the results above. For instance, the fields of M_0 , M_1 , M_2 , M_3 , and M_6 match within a maximum frequency error of 3% (see Table II), and the overall structures of the modes are captured well. This suggests that, despite the action of nonlinearities in the flow, the linear receptivity mechanisms that we have identified during the course of our analysis remain mostly intact and sustain the structures even through to the nonlinear regime, and even past the point of nonlinear saturation for the unstable modes. On the other hand, while having accurately predicted the set of dominant modes, identifying the most dominant tonal noise peak with frequency $\lambda_i = 31.57$ in Fig. 3 has proven to be a greater challenge with the field corresponding to M_1 rather than M_0 , which is otherwise suggested by a more positive real part of the selected eigenvalue. With the tools presented in this paper, identifying the causes of this change is difficult, and a more detailed analysis is required.

The linear and nonlinear models similarly agree on the compactness of the tonal-noise phenomena with the leading modes confined to the interval $|\text{Im}\{\lambda\}| \in [20, 80]$, which is precisely the region seen in the nonlinear analysis in the frequency domain. Despite this, it would be unwise to generalize this finding to arbitrary configurations, since the appearance of other small-scale features (like separation bubbles near the leading edge) will create additional high-frequency sources that must be captured with much finer meshes in order to resolve the corresponding instabilities.

F. Phase and group velocity analysis

One final question that we wish to address in this section is how the modes in Fig. 14 are related to each other, and whether they superpose to form larger structures that dominate the global dynamics. To this end, direct modes are first filtered by taking into account only those with convergence errors E less than 1×10^{-3} , which leaves 156 modes with nonzero frequencies, shown in Fig. 23(a).

The instantaneous wave number, k , of each mode is computed using a Pisarenko harmonic decomposition (PHD), which is a super-resolution method for frequency calculation of signals contaminated with noise. These calculations are performed by constructing a series of perpendicular contours in the regions upstream and downstream of the blade, as shown in Fig. 23(b), onto

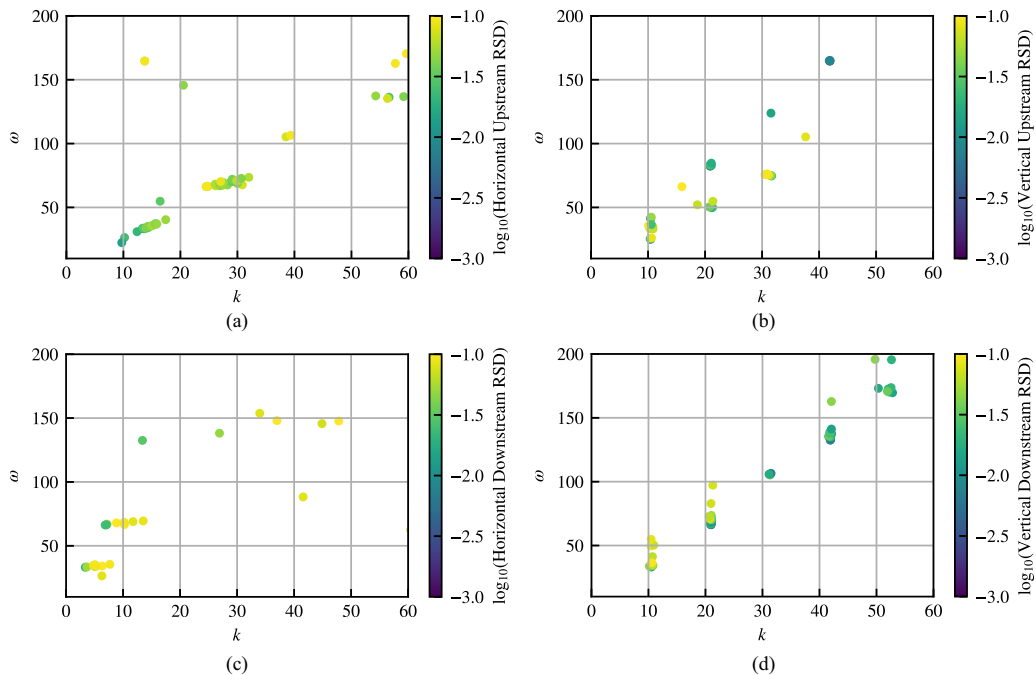


FIG. 24. The dispersion relation for each type of contour. Modes are filtered according to the standard deviation of the instantaneous wave number along the contour so that only the monochromatic modes with nonzero k are registered, and the average k is computed. Coloring of these modes is by relative standard deviation (RSD) of k .

which the acoustic field for the calculation is interpolated. To automate the process, the exact form of each mode is not assumed *a priori*, and so two additional parallel contours are used at each point in each direction to minimize the possibility that the contour falls into a node of the acoustic field which would not correctly identify erroneous frequencies.

The contours are subdivided into 60 equispaced arc-length segments with a two-dimensional piecewise cubic spline using the Clough-Tocher scheme (see `scipy interpolate` documentation [59]) interpolating the grid data onto this new contour. As a result, the Nyquist frequency is $k_n = 50$. The PHD is applied to this equispaced contour with two complex exponentials. From our earlier observations in Sec. III E 1 and in manual inspections of these modes, we observed that the pressure field in the regions surrounding the contours tends to be relatively regular and exhibits a dominant wave number in its structure. Consequently, we make the assumption that the instantaneous frequency should be constant along each of the contours, and so for each mode and contour we average to obtain the corresponding averaged wave number, along with the relative standard deviation/coefficient of variance (RSD/CV), c_v of the raw data. The resulting dispersion relations are plotted below for each type of contour where $c_v < 0.1$ in Fig. 24. For each of these we observe two dominant features. First, groups of modes occur in tight clusters with similar phase velocities, $v_p = \omega/k$, and, secondly, for almost all the modes there is a constant group velocity, $v_g = d\omega/dk$, confirming that these modes form a large structure under superposition that propagates together.

Identification of modes with consistent phase velocities is performed using the density-based clustering algorithm DBSCAN [60], which is able to identify clusters of modes based on the density of the data as well as being robust to outlying points. Applying this to the contours in Fig. 24(a) and Fig. 24(b), where the clustering of the modes is most visible, we obtain the following clusters, in Fig. 25, from which it appears that M_1 , M_2 , and M_3 (along with their axial resonant structures)

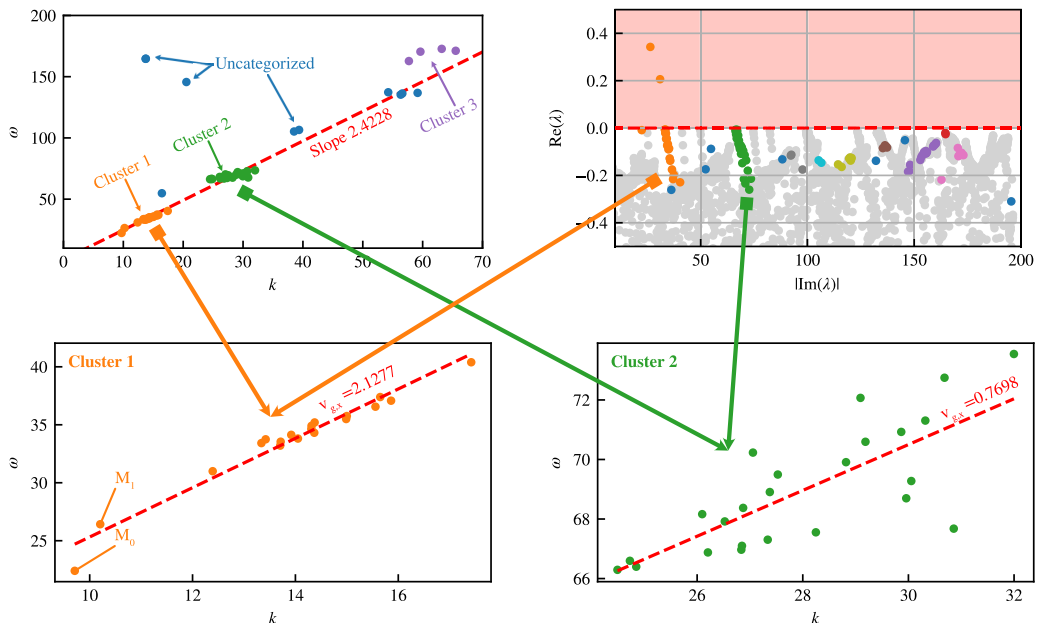


FIG. 25. Illustration of the clustering of the modes obtained with DBSCAN, the corresponding modes and detailed $k - \omega$ plots of the two main clusters identified in this analysis.

propagate as one, with the other modes superposing to form a large wave packet as a result of the constant group velocity. It is important to remember, however, that the disparate growth rates of the modes within this structure mean that most of the modes will decay quickly, leaving only the superposition of M_0 and M_1 , at least in the linear regime.

On the other hand, in the nonlinear case we have seen that the growth rates of the modes are not necessarily a good way of predicting which modes are selected by the nonlinear processes. Instead, those with the sensitive wavemakers are the ones that appear able to sustain the dynamics into the nonlinear regime.

IV. CONCLUSION

This paper considered the modal and nonmodal aeroacoustic stability properties of a representative linear compressor cascade at $Re = 100\,000$ and $M = 0.3$. It used a controlled-diffusion geometry that was adapted from earlier aeroelasticity experiments, and features an unstable suction-side laminar separation bubble that sheds vortices downstream to the trailing edge.

In the first part of this paper, a mean-flow global stability analysis was performed on a single-passage periodic domain. A transient response analysis highlighted regions of instability on the suction side, as well as a convectively unstable region on the pressure surface. The linear system was seen to be asymptotically unstable, and the mechanism for this instability was shown to manifest itself through a feedback process that links the upstream-propagating acoustic waves, originating at the trailing edge, to the sensitive boundary layers at the separation point of the laminar separation bubble.

A global stability analysis was then carried out, following which it was determined that the spectrum of the linear operator is unstable and characterized by two unstable and a sequence of 12 marginally stable modes, with the mode shapes and frequencies found to match very well with the pressure spectrum obtained from the nonlinear solution using the fast Fourier transform (FFT). From this it was also shown that the main peak in the pressure spectrum corresponds to the second-most unstable mode.

Through an analysis of the eigenvectors for these fourteen modes, three main groups of modes were identified. These were the Kelvin-Helmholtz modes, that drive the dominant dynamics of the system; high-frequency modes related to the separation bubble dynamics; and two degenerate modes, which were found in association with acoustic resonances within the blade passage.

To augment this description, adjoint modes were calculated. These confirmed that for the most unstable modes, the sensitivities were located upstream of the separation bubble, and also on the pressure surface for the most unstable modes. Applying the wavemaker concept, the structural sensitivities showed that the dominant dynamics of this system are determined by feedback processes involving the separation bubble and, more interestingly, the convectively unstable pressure-side region near the leading edge. This region is not linked convectively to the suction-side separation bubble and so the feedback mechanism occurs through acoustic means.

In many ways the single-passage results here can be seen to mirror earlier studies with isolated aerofoils. For example, much like the numerical studies [28,29] and the global stability analyses conducted [12,13] for the NACA-0012 aerofoil, the linear cascade is shown to have similar receptivity and sensitivity characteristics on the pressure and suction surfaces of the blade, with aeroacoustic feedback mechanisms shown to exploit these sensitivities. The generated acoustics field also shares considerable similarities and characteristics to the isolated CD aerofoil studies at similar flow conditions [30,31], especially with respect to the characteristics of the acoustic source and the upstream directivity of the propagating acoustic waves. Of course, the exact properties of the flow change due to the presence of the cascade, with the separation bubble located approximately midchord instead of near the leading or trailing edges, and the global instability to impulse perturbations remains. Unlike earlier work with isolated aerofoils, however, this case also captures features such as acoustic resonances in the blade passage and pressure-side instabilities. By making use of the direct-adjoint methodology provided to us by this framework, we can also be more definitive about the nature and origin of the processes that sustain the aeroacoustic feedback loop, compared to purely numerical studies that have to infer the feedback mechanisms from nonlinear time-series data. Furthermore, such global stability analyses have rarely been applied, with one of the few works by [56] applying this analysis to high-pressure turbine flows, and so this work provides insight into the cascade problem.

Despite the simplifications and modeling assumptions introduced to the flow configurations considered here, this work nevertheless serves to demonstrate the very real shortcomings inherent in local analyses used in many current turbomachinery design methodologies. Instead, it has been shown here that these systems are dominated by *networks* of instabilities, where flow fluctuations in one part of the domain drive other structures elsewhere, through interaction pathways that are otherwise very difficult to separate by means of a purely local analysis. The change from this two-dimensional model to the real machinery will introduce additional flow features that would only increase the complexity of these networks, thereby magnifying the need of this kind of global approach as part of the analysis at the design stage.

ACKNOWLEDGMENTS

The authors gratefully acknowledge financial support from Ministerio de Economía y Competitividad AEI/FEDER UE through Grant No. DPI2016-75777-R, as well as computer resources at FinisTerra II and the technical support provided by CESGA (IM-2019-3-0013 and IM-2020-1-0024). This work also used the ARCHER and ARCHER2 UK National Supercomputing Service.

APPENDIX A: NUMERICAL DETAILS—NEAR-WAKE NORMALIZATION REGION FOR GLOBAL MODES

All direct global modes in this paper are normalized by the near-wake axial-velocity component, u , of the state vector. This choice is made because, for most modes here, the dynamics of the mode are driven by a self-excited instability that generates a wake that is convected downstream of the

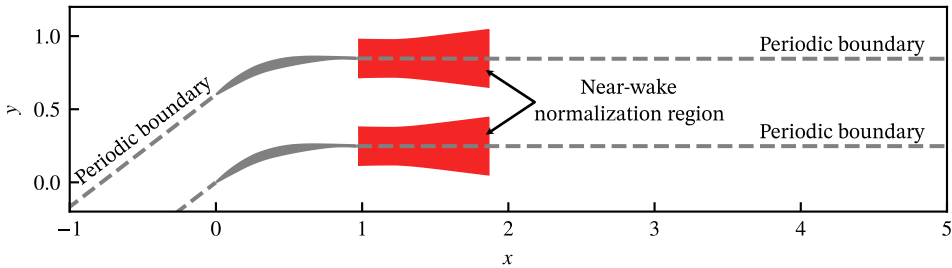


FIG. 26. The near-wake normalization region for the global modes.

trailing edge. By performing the normalization on these wake structures, and considering modes describing similar dynamics, a comparative analysis of the mode structures can be performed.

Since the normalization procedure has to account for multiple-blade passages, the region in which the normalization is performed is made compact, so that one blade wake is selected at a time. To simplify the procedure, the closed downstream region, bounded by the grid lines $n_y = \pm 100$, $n_x = 1081$ and $n_x = 1281$, is selected, thereby avoiding interpolation and complex array slicing. This yields a region with an initial height of $\Delta y \approx 0.77$ centered vertically on the trailing edge, and extending for $\Delta x \approx 1.35$ before expanding as a trapezoid until $x \approx 1.87$, with a final height of $\Delta y \approx 0.95$. This is shown in Fig. 26.

-
- [1] N. Peake and A. B. Parry, Modern challenges facing turbomachinery aeroacoustics, *Annu. Rev. Fluid Mech.* **44**, 227 (2012).
 - [2] P. J. Schmid, Nonmodal stability theory, *Annu. Rev. Fluid Mech.* **39**, 129 (2007).
 - [3] K. Taira, S. L. Brunton, S. T. M. Dawson, C. W. Rowley, T. Colonius, B. J. McKeon, O. T. Schmidt, S. Gordeyev, V. Theofilis, and L. S. Ukeiley, Modal analysis of fluid flows: An overview, *AIAA J.* **55**, 4013 (2017).
 - [4] J. L. Lumley, The Structure of Inhomogeneous Turbulent Flows, in *Proceedings of the International Colloquium on the Fine Scale Structure of the Atmosphere and Its Influence on Radio Wave Propagation*, edited by A. M. Yaglam and V. I. Tatarsky (Doklady Akademii Nauk SSSR, Nauka, Moscow, 1967).
 - [5] P. J. Schmid, Dynamic mode decomposition of numerical and experimental data, *J. Fluid Mech.* **656**, 5 (2010).
 - [6] K. Taira, M. S. Hemati, S. L. Brunton, Y. Sun, K. Duraisamy, S. Bagheri, S. T. M. Dawson, and C.-A. Yeh, Modal analysis of fluid flows: Applications and outlook, *AIAA J.* **58**, 998 (2020).
 - [7] P. J. Schmid and D. S. Henningson, *Stability and Transition in Shear Flows*, Applied Mathematical Sciences Vol. 142 (Springer, New York, 2001).
 - [8] S. Beneddine, D. Sipp, A. Arnault, J. Dandois, and L. Lesshafft, Conditions for validity of mean flow stability analysis, *J. Fluid Mech.* **798**, 485 (2016).
 - [9] M. P. Juniper, Absolute and Convective Instability in Gas Turbine Fuel Injectors, in *Proceedings of the ASME Turbo Expo 2012: Turbine Technical Conference and Exposition. Volume 2: Combustion, Fuels and Emissions, Parts A and B. Copenhagen, Denmark* (American Society of Mechanical Engineers, 2012), pp. 189–198.
 - [10] O. Tammisola and M. P. Juniper, Coherent structures in a swirl injector at $Re = 4800$ by nonlinear simulations and linear global modes, *J. Fluid Mech.* **792**, 620 (2016).
 - [11] K. Gudmundsson and T. Colonius, Instability wave models for the near-field fluctuations of turbulent jets, *J. Fluid Mech.* **689**, 97 (2011).
 - [12] M. Fosas de Pando, P. J. Schmid, and D. Sipp, A global analysis of tonal noise in flows around aerofoils, *J. Fluid Mech.* **754**, 5 (2014).

- [13] M. Fosas de Pando, P. J. Schmid, and D. Sipp, On the receptivity of aerofoil tonal noise: An adjoint analysis, *J. Fluid Mech.* **812**, 771 (2017).
- [14] D. C. Hill, A theoretical approach for analyzing the restabilization of wakes, Tech. Rep., NASA Technical Memorandum 103858, Ames Research Center, 1992.
- [15] F. Giannetti and P. Luchini, Structural sensitivity of the first instability of the cylinder wake, *J. Fluid Mech.* **581**, 167 (2007).
- [16] J. Chomaz, Global instabilities in spatially developing flows: Non-normality and nonlinearity, *Annu. Rev. Fluid Mech.* **37**, 357 (2005).
- [17] P. J. Schmid and L. Brandt, Analysis of fluid systems: Stability, receptivity, sensitivity, *Appl. Mech. Rev.* **66**, 024803 (2014).
- [18] D. X. Wang and L. He, Adjoint aerodynamic design optimization for blades in multistage turbomachines—Part I: Methodology and verification, *J. Turbomach.* **132**, 021011 (2010).
- [19] D. X. Wang, L. He, Y. S. Li, and R. G. Wells, Adjoint aerodynamic design optimization for blades in multistage turbomachines—Part II: Validation and application, *J. Turbomach.* **132**, 021012 (2010).
- [20] A. Jameson, Aerodynamic design via control theory, *J. Sci. Comput.* **3**, 233 (1988).
- [21] M. B. Giles and N. A. Pierce, An introduction to the adjoint approach to design, *Flow, Turbul. Combust.* **65**, 393 (2000).
- [22] L. N. Trefethen and D. Bau III, *Numerical Linear Algebra* (SIAM, Philadelphia, 1997).
- [23] R. W. Paterson, P. G. Vogt, M. R. Fink, and C. Lee Munch, Vortex noise of isolated airfoils, *J. Aircr.* **10**, (1973).
- [24] C. K. W. Tam, Discrete tones of isolated airfoils, *J. Acoust. Soc. Am.* **55**, 1173 (1974).
- [25] M. R. Fink, Prediction of airfoil tone frequencies, *J. Aircr.* **12**, (1975).
- [26] E. C. Nash, M. V. Lowson, and A. McAlpine, Boundary-layer instability noise on aerofoils, *J. Fluid Mech.* **382**, 27 (1999).
- [27] S. Pröbsting, J. Serpieri, and F. Scarano, Experimental investigation of aerofoil tonal noise generation, *J. Fluid Mech.* **747**, 656 (2014).
- [28] G. Desquesnes, M. Terracol, and P. Sagaut, Numerical investigation of the tone noise mechanism over laminar airfoils, *J. Fluid Mech.* **591**, 155 (2007).
- [29] L. E. Jones and R. D. Sandberg, Numerical analysis of tonal airfoil self-noise and acoustic feedback-loops, *J. Sound Vib.* **330**, 6137 (2011).
- [30] M. Sanjose, A. Towne, P. Jaiswal, S. Moreau, S. Lele, and A. Mann, Modal analysis of the laminar boundary layer instability and tonal noise of an airfoil at Reynolds number 150,000, *Intl. J. Aeroacoustics* **18**, 317 (2019).
- [31] H. Wu, R. D. Sandberg, and S. Moreau, Stability characteristics of different aerofoil flows at $Re_c = 150,000$ and the implications for aerofoil self-noise, *J. Sound Vib.* **506**, 116152 (2021).
- [32] A. Glazkov, M. F. de Pando, P. J. Schmid, and L. He, following paper, Global stability analysis of an idealized compressor blade row. II. Multiple-blade interactions, *Phys. Rev. Fluids* **8**, 103904 (2023).
- [33] P. J. Schmid, M. F. de Pando, and N. Peake, Stability analysis for n -periodic arrays of fluid systems, *Phys. Rev. Fluids* **2**, 113902 (2017).
- [34] N. L. Sanger and R. P. Shreeve, Comparison of calculated and experimental cascade performance for controlled-diffusion compressor stator blading, *J. Turbomach.* **108**, 42 (1986).
- [35] T. Sasaki and F. Breugelmans, Comparison of sweep and dihedral effects on compressor cascade performance, *J. Turbomach.* **120**, 454 (1998).
- [36] H. Yang and L. He, Experimental study on linear compressor cascade with three-dimensional blade oscillation, *J. Propul. Power* **20**, (2004).
- [37] L. He and J. Yi, Two-scale methodology for URANS/Large Eddy Simulation solutions of unsteady turbomachinery flows, *J. Turbomach.* **139**, 101012 (2017).
- [38] L. He, Averaging for high fidelity modeling—Toward large eddy simulations in multi-passages multi-row configurations, *J. Turbomach.* **143**, 021002 (2021).
- [39] A. Glazkov, A direct-adjoint framework for stability and sensitivity analyses of turbomachinery aeroacoustics, Ph.D. thesis, University of Oxford, 2021.

- [40] J. Sesterhenn, A characteristic-type formulation of the Navier-Stokes equations for high order upwind schemes, *Comput. Fluids* **30**, 37 (2000).
- [41] M. Fosas de Pando, Tonal noise generation in flows around aerofoils: A global stability analysis, Ph.D. thesis, École Polytechnique, 2012.
- [42] N. A. Adams and K. Shariff, A high-resolution hybrid compact-ENO scheme for shock-turbulence interaction problems, *J. Comput. Phys.* **127**, 27 (1996).
- [43] S. K. Lele, Compact finite difference schemes with spectral-like resolution, *J. Comput. Phys.* **103**, 16 (1992).
- [44] C. A. Kennedy, M. H. Carpenter, and R. M. Lewis, Low-storage, explicit Runge-Kutta schemes for the compressible Navier-Stokes equations, *Appl. Numer. Math.* **35**, 177 (2000).
- [45] MPI Forum, <https://www.mpi-forum.org/> (2021).
- [46] M. Fosas de Pando, D. Sipp, and P. J. Schmid, Efficient evaluation of the direct and adjoint linearized dynamics from compressible flow solvers, *J. Comput. Phys.* **231**, 7739 (2012).
- [47] S. Abhyankar, J. Brown, E. M. Constantinescu, D. Ghosh, B. F. Smith, and H. Zhang, PETSc/TS: A modern scalable ODE/DAE solver library, [arXiv:1806.01437](https://arxiv.org/abs/1806.01437).
- [48] S. Balay, S. Abhyankar, M. F. Adams, J. Brown, P. Brune, K. Buschelman, L. Dalcin, A. Dener, V. Eijkhout, W. D. Gropp *et al.*, PETSc user's manual, Tech. Rep. ANL-95/11, Revision 3.13, Argonne National Laboratory, 2020.
- [49] S. Balay, S. Abhyankar, M. F. Adams, J. Brown, P. Brune, K. Buschelman, L. Dalcin, A. Dener, V. Eijkhout, W. D. Gropp *et al.*, PETSc Web page, <https://www.mcs.anl.gov/petsc> (2019).
- [50] V. Hernandez, J. E. Roman, and V. Vidal, SLEPc, *ACM Trans. Math. Softw.* **31**, 351 (2005).
- [51] E. Åkervik, L. Brandt, D. S. Henningson, J. Høpfner, O. Marxen, and P. Schlatter, Steady solutions of the Navier-Stokes equations by selective frequency damping, *Phys. Fluids* **18**, 068102 (2006).
- [52] J. Crouch, A. Garbaruk, and D. Magidov, Predicting the onset of flow unsteadiness based on global instability, *J. Comput. Phys.* **224**, 924 (2007).
- [53] B. T. Chu, On the energy transfer to small disturbances in fluid flow (Part I), *Acta Mech.* **1**, 215 (1965).
- [54] J. C. Schulze, P. J. Schmid, and J. L. Sesterhenn, Exponential time integration using Krylov subspaces, *Int. J. Numer. Methods Fluids* **60**, 591 (2009).
- [55] Lord Rayleigh, On the stability, or instability, of certain fluid motions, *Proc. London Math. Soc.* **s1-11**, 57 (1879).
- [56] R. Sandberg and A. Wheeler, Effect of trailing-edge boundary conditions on acoustic feedback loops in high-pressure turbines, *J. Sound Vib.* **461**, 114917 (2019).
- [57] R. Parker, Resonance effects in wake shedding from compressor blading, *J. Sound Vib.* **6**, 302 (1967).
- [58] B. Hellmich and J. R. Seume, Causes of acoustic resonance in a high-speed axial compressor, *J. Turbomach.* **130**, 031003 (2008).
- [59] <https://docs.scipy.org/doc/scipy/reference/interpolate.html>.
- [60] M. Hahsler, M. Piekenbrock, and D. Doran, dbscan: Fast density-based clustering with R, *J. Stat. Softw.* **91**, 1 (2019).